Available online at www.sciencedirect.com

ScienceDirect

Advances in Space Research 72 (2023) 2627–2648

ADVANCES IN SPACE RESEARCH (a COSPAR publication)

www.elsevier.com/locate/asr

Intelligent decision support for collision avoidance manoeuvre planning under uncertainty

Luis Sánchez, Massimiliano Vasile *

Aerospace Centre of Excellence, University of Strathclyde, Glasgow, United Kingdom

Received 4 February 2022; received in revised form 6 September 2022; accepted 11 September 2022
Available online 20 September 2022

Abstract

This paper presents a decision support system that can automatically allocate collision avoidance manoeuvres in the event of a high risk close encounter between two space objects. Decisions are supported by an Intelligent Classification System that combines Dempster-Shafer theory of evidence with Machine Learning to automatically classify conjunctions according to the probability of collision, the uncertainty on the probability of collision, the time to close approach and the cost of a collision avoidance manoeuvre. We propose a simple analytical model that allows for the fast and robust computation of both impulsive and low-thrust manoeuvres under a mix of aleatory and epistemic uncertainty. Aleatory uncertainty is the non-reducible randomness in observation data, dynamic model and parameters, while epistemic uncertainty is the lack of knowledge on system dynamics and observation data, including the model of aleatory uncertainty itself. Dempster-Shafer theory of evidence is used to model the epistemic uncertainty in the calculation of the probability of collision. Some numerical examples are included to show the performance of the collision avoidance manoeuvre optimisation strategy and of the intelligent decision support system.
© 2022 COSPAR. Published by Elsevier B.V. This is an open access article under the CC BY license (http://creativecommons.org/licenses/by/4.0/).

Keywords: Collision avoidance manoeuvre; Machine learning; Min-max optimisation; Epistemic uncertainty; Low-thrust; Decision-making

1. Introduction

In recent years, the so called New Space movement and more generally the rapid growth of the private space sector have led to an increase in traffic in orbit. This increase in traffic requires a paradigm shift in the way operators manage space assets Muelhaupt et al. (2019).

The growth in the number of tracked space objects, both operational and non-operational, means an increase in the number of conjunction alerts to be addressed by the operator. Currently, space conjunctions trigger hundreds of alerts per year. Although the vast majority of them are associated to non-critical events, a space environment several times more populated may saturate the current Space Traffic Management (STM) capabilities, as the assessment of high-risk events is time consuming and requires substantial operational resources. Furthermore, it is expected that the rise of the number of close encounters will translate into a higher number of alerts accompanied by an increased difficulty in differentiating between high and low risk events. Ultimately, the overall safety of operations in space Peterson et al. (2018) could be compromised.

If the event involves two operational satellites, the situation becomes even more critical because of the lack of clear protocols, automated communications and tasks Nag et al. (2018). Finally, even if the Collision Avoidance Manoeuvres (CAMs) are not expensive, in comparison with other satellite's operations, an increase in the number of manoeuvres will increase the total amount of propellant on board and the cumulative disruption of nominal opera-

* Corresponding author at: James Weir Building, 75 Montrose St., G1 1XJ Glasgow, United Kingdom.
E-mail address: massimiliano.vasile@strah.ac.uk (M. Vasile).

https://doi.org/10.1016/j.asr.2022.09.023
0273-1177/© 2022 COSPAR. Published by Elsevier B.V.
This is an open access article under the CC BY license (http://creativecommons.org/licenses/by/4.0/).

tions. Therefore, a better assessment of collision risk and the automation of operations have become a necessity Nag et al. (2021). Automation can help making robust decisions on collision risk and CAM execution, by processing large volumes of data and speeding up decision tasks. Enhancing robustness in decision making requires dealing with both aleatory and epistemic uncertainty and managing different sources of information potentially incomplete or conflicting.

In this paper, we address three main aspects. Firstly, the robust assessment of collision risk by the integrated treatment of both aleatory and epistemic uncertainty in the computation of the collision risk and CAM optimisation. Secondly, the automation of the decision-making process by the introduction of an Intelligent Classification System (ICS) that can provide a fast and robust classification of conjunction events. And finally, the robust and quick optimisation of CAM by the development of a linear model for computing both impulsive and Low-Thrust (LT) manoeuvres.

This paper builds on previous work by the authors where the ICS was introduced Sánchez et al. (2019), Sánchez and Vasile (2021). The ICS is based on a Random Forests (RF) algorithm for data classification. The use of Machine Learning (ML) in the field of STM has gained popularity in recent years. Peng and Bai Peng and Bai (2017), Peng and Bai (2018b), Peng and Bai (2018a) used Artificial Neural Networks (ANN) and Support Vector Machine to reduce the error on the orbit propagation, Vasile *et al.* Vasile et al. (2017) introduced a ML-based model for analysing the collision risk and evaluating the CAM strategy, Stevenson *et al.* Stevenson et al. (2021) used a Deep Learning-based approach for assessing the many-vs-many conjunction problem. Space agencies like NASA and ESA have demonstrated a keen interest in this line of developments, for example Nag et al. (2018), Mashiku et al. (2018, 2019), or the ESA's CREAM program Bastida Virgili et al. (2019) and the recent ESA challenge on collision risk prediction ESA (2019), Uriot et al. (2022), Tulczyjew et al. (2020).

Relevant to the current paper, some works have been also published on the use of ML for automatic CAM Gonzalo et al. (2020), Abay et al. (2017). It is interesting to note that those works are based on analytical or semi-analytical approaches to compute the optimal CAM. For the impulsive case, different analytical models have been developed all of them based on the idea of the impulses being small enough to be linearly approximated Vasile et al. (2017), Sánchez and Vasile (2020), Bombardelli and Hernando-Ayuso (2015), Abay (2017). Some of those models come from the theory of asteroid deflection Vasile and Colombo (2008). Some efforts have been also put on developing similar semi-analytical models for the LT case Hernando-Ayuso and Bombardelli (2020), Gonzalo et al. (2019).

However, a common denominator of most of these publications is the lack of a specific model of epistemic uncertainty. The uncertainty is usually only modelled as purely aleatory, even when it is not, possibly leading to the well-known counter-intuitive phenomenon of the dilution of probability Alfano (2004). As shown in Balch et al. (2019), epistemic uncertainty plays an important role and needs a dedicated treatment. In this paper, we use Dempster-Shafer theory of evidence (DSt) Shafer (1976) for modelling both aleatory and epistemic uncertainty. DSt allows one to assess the risk of collision accounting for all sources of information and pieces of evidence.

The rest of the paper is structured as follows: in Section 2 we introduce the linear models used to compute an optimal CAM, both impulsive and low thrust, accounting for both aleatory and epistemic uncertainty; Section 3 presents a revised ICS that accounts for CAM execution; in Section 4, some case studies are presented to test the linear model under different conditions and to show the performance of the ICS at proposing the most suitable action; finally Section 5 contains some concluding remarks and future recommendations.

2. Collision avoidance manoeuvre models

This section introduces the linear models that will be used to compute the CAM both with an impulsive Δv and with a low-thrust arc. The section will then present a method for the optimisation of CAMs accounting for both aleatory and epistemic uncertainty.

2.1. Linear model for impulsive manoeuvres

This section briefly presents the linear model, developed in Sánchez and Vasile (2020) and initially proposed in Vasile et al. (2017), to compute the impulsive manoeuvre to achieve the desired variation of the relative position between a manoeuvrable object (the primary) and another object (the secondary), which may or may not have manoeuvre capabilities (in this paper we assume that the target is not manoeuvrable), which experience a close encounter (Fig. 1a).

Given a manoeuvre $\delta\mathbf{v}$, at time t_m, expressed in a spacecraft centred tangential, normal, out-of-plane reference frame, <T,N,H> (Fig. 1c), the corresponding variation of position $\delta\mathbf{x}_b$ at time t_c on the target's impact plane (or b-plane), $<\xi,\eta,\zeta>$, is:

$$\delta\mathbf{x}_b = [\delta\xi \;\; \delta\eta \;\; \delta\zeta]^T = \mathbf{T}\delta\mathbf{v} = \mathbf{B}\mathbf{A}(t_m,t_c)\mathbf{G}\delta\mathbf{v} \tag{1}$$

where matrix $\mathbf{T}$ is the product of three matrices: i) $\mathbf{G}$ relating the instantaneous change in orbital parameters due to the change in velocity at the time of execution of the manoeuvre, ii) $\mathbf{A}(t_m,t_c)$ being the transition matrix between the variation of the Keplerian elements at manoeuvre, t_m, and the variation of the relative position at the time of expected collision, t_c, expressed in a radial, transversal, out-of-plane reference frame, <R,T,H>, iii) and $\mathbf{B}$ the rotation matrix between <R,T,H> and the impact plane

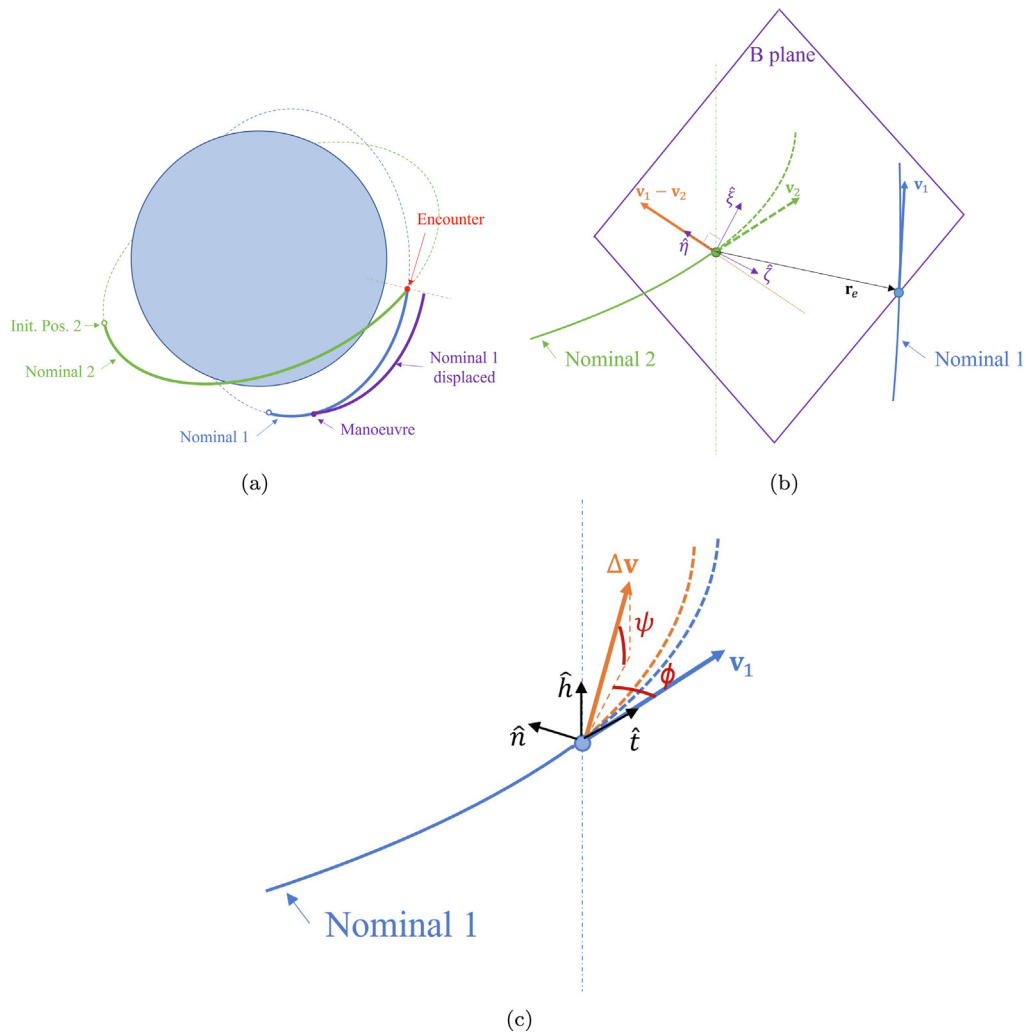

Fig. 1. (a) General configuration of the encounter. Blue: nominal primary object's orbit, green: nominal secondary object's orbit, purple: manoeuvre and nominal primary object's orbit after CAM. Red: encounter position. The encounter and manoeuvre positions are detailed on the subsequent figures. (b) Encounter configuration. Blue: primary object (trajectory and orbital velocity, $\mathbf{v}_1$), green: secondary object (trajectory and orbital velocity, $\mathbf{v}_2$), black: miss distance ($\mathbf{r}_e$), orange: relative velocity, purple: impact plane and its reference frame $< \xi, \eta, \zeta >$. (c) Manoeuvre position. Blue: primary object's orbit (trajectory and orbital velocity, $\mathbf{v}_1$), orange: impulsive manoeuvre ($\Delta\mathbf{v}$), red: angles between orbital velocity and impulse (ϕ in plane, ψ out of plane), black: primary object's <T,N,H> reference frame.

reference frames. More details can be found in Sánchez and Vasile (2020) and Vasile and Colombo (2008).

The direction of the impulse can be defined by the two angles $\phi \in [-\pi, \pi]$ and $\psi \in [-\pi/2, \pi/2]$ (see Fig. 1c). The relation between $[\phi, \psi]$ and the components on the <T,N, H > is:

$$\begin{aligned} \phi &= \arctan\left((\mathbf{v}_1 \times \delta\mathbf{v}) \cdot \mathbf{u}_{1h}, \mathbf{v}_1 \cdot \delta\mathbf{v}\right) \\ \psi &= \arctan\left[\frac{(\delta\mathbf{v}\cdot\mathbf{u}_{1h})\|\delta\mathbf{v}\times\mathbf{u}_{1h}\|}{\delta v^2 - (\delta\mathbf{v}\cdot\mathbf{u}_{1h})^2}\right] \end{aligned} , \tag{2}$$

with $\mathbf{u}_{1h}$ the normal to the primary object's orbital plane, and the arc-tangent is computed taking care of quadrant discrimination. Note that the model in Eq. 1 assumes Keplerian motion. The orbital parameters and positions included in the expressions of the matrices refer to the manoeuvrable object (the chaser) while the impact plane reference frame $<\xi, \eta, \zeta>$ is centred at the secondary object (the target), and is defined as:

$$\hat{\boldsymbol{\eta}} = \frac{\mathbf{v}_1 - \mathbf{v}_2}{\|\mathbf{v}_1 - \mathbf{v}_2\|}, \quad \hat{\boldsymbol{\xi}} = \frac{\mathbf{v}_2 \times \boldsymbol{\eta}}{\|\mathbf{v}_2 \times \boldsymbol{\eta}\|}, \quad \hat{\boldsymbol{\zeta}} = \hat{\boldsymbol{\xi}} \times \hat{\boldsymbol{\eta}} \tag{3}$$

where $\mathbf{v}_1$ is the velocity vector of the chaser and $\mathbf{v}_2$ the velocity vector of the target (see Fig. 1b).

2.2. Optimisation of impulsive manoeuvres under aleatory uncertainty

In this section, the method to compute the optimal CAM under uncertainty is presented. First, only aleatory uncertainty is considered. Taking $\mathbf{r}_{e_0} = [\xi_0, 0, \zeta_0]^T$, the initial unmodified relative position between both objects projected on the impact plane defined in the previous section, with combined covariance matrix $\boldsymbol{\Sigma}$, the optimal CAM can

be computed so that the Probability of Collision (PoC) is minimised. The combined covariance matrix is the sum of both object's position covariance matrices projected on the impact plane of the target: $\mathbf{\Sigma} = \mathbf{\Sigma}_{1_{Bp}} + \mathbf{\Sigma}_{2_{Bp}}$.

We assume that the manoeuvre introduces a negligible uncertainty and that it only translates rigidly the uncertain ellipse on the impact plane, defined by the combined covariance matrices, not modifying its shape, size or orientation. This means that the relative position of the modified orbit will present the same covariance matrix $\mathbf{\Sigma}$, with miss distance equal to $\mathbf{r}_e = \mathbf{r}_{e_0} + \delta\mathbf{x}_b$, and $\delta\mathbf{x}_b$ given by Eq. 1. Furthermore, we introduce the short-encounter assumptions defined in Serra et al. (2016): i) rectilinear relative trajectories, ii) no uncertainty in the velocity vector, iii) the uncertainty in the position of the two objects is Gaussian and uncorrelated, iv) and the shape of the two objects is spherical. Under these conditions, the PoC computation can be approximated as the 2D integral:

$$P_C = \frac{1}{2\pi\sqrt{\|\overline{\mathbf{\Sigma}}\|}} \int_{\mathscr{B}((0,0),R)} e^{-\frac{1}{2}\left((\mathbf{b}-\bar{\mathbf{r}}_e)^T\overline{\mathbf{\Sigma}}^{-1}(\mathbf{b}-\bar{\mathbf{r}}_e)\right)} d\xi d\zeta \tag{4}$$

where $\mathscr{B}((0,0),R)$ is the integration region centred at the secondary object with radius equal to the Hard-Body Radius (HBR), the radius of the sphere enveloping the two objects; $\mathbf{b} = [\xi, \zeta]^T$; the two component vector $\bar{\mathbf{r}}_e$ is equal to the first and third components of $\mathbf{r}_e$; and $\overline{\mathbf{\Sigma}}$ is a 2×2 matrix equal to the first and third elements of the first and third rows of $\mathbf{\Sigma}$:

$$\overline{\mathbf{\Sigma}} = \begin{bmatrix} \sigma_\xi^2 & \sigma_{\xi\zeta} \\ \sigma_{\xi\zeta} & \sigma_\zeta^2 \end{bmatrix}.$$

Eq. 4 assumes that the area of the secondary object on the impact plane is the combined radial envelope of the areas of both objects projected on the same plane, while the combined uncertainty projected on the impact plane is associated to the primary object and centred in $\bar{\mathbf{r}}_e$. Under the assumption that the manoeuvre does not change the shape of the covariance, Eq. 4 is equivalent to placing the HBR centred in $\bar{\mathbf{r}}_e$ and the combined ellipse of uncertainty centred in (0,0) on the impact plane.

Then, in order to minimise the PoC, one needs to solve the following maximisation problem:

$$\begin{aligned} &\max_{\delta\mathbf{v}} \left(\delta\mathbf{v}^T \mathscr{T} \delta\mathbf{v} + 2\mathbf{r}_{e_0}\mathbf{\Sigma}^{-1}\mathbf{QT}\delta\mathbf{v}\right) \\ &s.t. \\ &\|\delta\mathbf{v}\| \leqslant \delta v_{max} \end{aligned} , \tag{5}$$

where $\mathscr{T} = \mathbf{QT}^T\mathbf{\Sigma}^{-1}\mathbf{TQ}$ and

$$\mathbf{Q} = \begin{bmatrix} 1 & 0 & 0 \\ 0 & 0 & 0 \\ 0 & 0 & 1 \end{bmatrix}$$

In the following, however, we fix the magnitude of the manoeuvre δv_0 and solve the simplified problem:

$$\begin{aligned} &\max_{\delta\mathbf{v}} (\delta\mathbf{v}^T \mathscr{T} \delta\mathbf{v}) \\ &s.t. \\ &\mathbf{r}_e \cdot \mathbf{T}\delta\mathbf{v} > 0 \end{aligned} , \tag{6}$$

whose solution $\delta\mathbf{v}_{opt}$ is the vector parallel to the eigenvector, $\mathbf{s_1}$, conjugate to the maximum eigenvalue of the matrix $\mathscr{T}$ with magnitude δv_0:

$$\delta\mathbf{v}_{opt} = \delta v_0 \mathbf{s_1} \tag{7}$$

2.3. Computation of the probability of collision under epistemic uncertainty

When the covariance matrix $\mathbf{\Sigma}$ or the miss distance are not precisely known the PoC is computed accounting for a degree of uncertainty. This uncertainty is epistemic in nature and can come from a lack of knowledge of the system dynamics, the distribution of measurements, the sensor, the propagation method, and the observation data. In this paper, we assumed that all these sources of uncertainty concur to define the epistemic uncertainty in covariance and miss distance but without entering in the details of the origin of the lack of knowledge. As presented in Sánchez and Vasile (2021) this epistemic uncertainty can be modelled with DSt Shafer (1976).

The idea proposed in Sánchez and Vasile (2021), is to use DSt to compute the level of confidence in the correctness of the value of the PoC, given the available evidence on the sources of information. Each component of the covariance, $\left[\sigma_\xi^2, \sigma_\zeta^2, \sigma_{\xi\zeta}\right]$, is modelled with one or more intervals and so is the mean value of the relative position $\left[\mu_\xi, \mu_\zeta\right]$. A basic probability assignment (bpa) is associated to each interval. Intervals and associated bpas can be derived, for example, from a time series of Conjunction Data Messages (CDMs) or directly from the raw observations Greco et al. (2021). In the former case we assumed that the values of covariance and miss distance in the series of CDMs belonged to an unknown family of distributions. Thus covariance and miss distance could not be modelled with a crisp value or with a single specific distribution.

Given the intervals and associated bpas, we compute the cross product of all the intervals, under the assumption of epistemic independence. Each product of intervals is a Focal Element (FE), and the associated bpa is the product of the bpas of the individual intervals. With the FEs we can compute the *Belief* (lower probability) and *Plausibility* (upper probability) that the PoC associated to a given conjunction event is correct. In the following we call the uncertainty space, U, and the uncertain parameter vector, $\mathbf{u} = \left[\mu_\xi, \mu_\zeta, \sigma_\xi^2, \sigma_\zeta^2, \sigma_{\xi\zeta}\right]^T$. We then want to compute the *Belief* and *Plausibility* of $\Phi = \left\{P_C | P_C \geqslant \overline{P_{C0}}\right\}$ where $\overline{P_{C0}}$ is a desirable value. Finally, we can define the set:

$$\Omega_u = \{\mathbf{u} \in U | f(\mathbf{u}) \in \Phi\}, \tag{8}$$

where $f(\mathbf{u})$ is a quantity of interest, in this case, the probability of collision defined in Eq. 4. For more information please refer to Sánchez and Vasile (2021).

2.4. Optimisation of impulsive collision avoidance manoeuvres under epistemic uncertainty

When epistemic uncertainty is considered, the PoC is not defined by a single ellipsoid but by families of ellipsoids corresponding to families of covariances and mean values. Thus, instead of having a single uncertain ellipse on the impact plane one has to consider families of uncertain ellipses each of which has to be displaced by a manoeuvre. This means that an optimal and robust manoeuvre has to displace all the ellipses at once.

Fig. 2 presents this situation where two families of uncertain ellipses (red and green) are shown on the impact plane, against a single ellipse (blue) obtained by combining the information from both sources and considering solely aleatory uncertainty.

The presence of families of ellipses means that the optimal CAM has to be able to minimised the PoC corresponding to the worst-case ellipse, which is the uncertain ellipse leading to the highest value of the PoC. Thus the minimisation problem presented in Section 2.2 needs to be reformulated into the following min-max problem:

$$\begin{aligned} &\min_{\delta\mathbf{v}} \max_{\mathbf{u}\in\Omega_u} P_C \\ &s.t. \qquad , \\ &\mathbf{r}_e \cdot \delta\mathbf{v} > 0 \end{aligned} \tag{9}$$

which has to be solved over the whole set of FEs. Problem 9 is a constrained robust optimisation problem where the optimal manoeuvre reduces the highest risk of a collision over the whole set of ellipses.

Similarly to what proposed in Filippi Filippi and Vasile (2019) for the solution of general min-max optimisation problems, we propose the following iterative process. First we compute for each FE the value of the uncertainty vector that gives the highest PoC. We then build the matrix $\mathbf{S} = \mathbf{\Sigma}_1^{-1} + \mathbf{\Sigma}_2^{-1} + \dots$ given by the sum of all the worst-case ellipses for all FEs. From $\mathbf{S}$ we compute $\mathscr{T}$ and then use Eq. 7 to compute the manoeuvre.

Since the implementation of a manoeuvre displaces all the ellipses, the process has to be repeated until there is no variation of the PoC. The pseudo-code of the min-max algorithm can be found in Algorithm 1.

2.4.1. Optimisation of the impulse magnitude

Up to this point, the optimisation of the manoeuvre assumed a constant magnitude, δv_0. However, this can lead to situations where the correction of the orbit is overestimated, with a reduction of the PoC several orders of magnitude below the minimum safety threshold. In such situation, a smaller impulse could reduce the risk to acceptable levels without an excessive cost of the manoeuvre.

Assuming the maximum capacity of the thruster is defined by δv_{max}, the optimum value of the magnitude will be the minimum one that allows reducing the worst-case scenario PoC below the selected threshold, P_{C0}:

$$\begin{aligned} &\min \quad \|\delta\mathbf{v}\| \\ &\text{s.t.} \quad P_C < P_{C0}, \end{aligned} \tag{10}$$

Once the optimal direction is computed with Eq. 7, the minimum δv can be simply derived from the solution of problem (10). However, since the magnitude of the impulse affects the deflection of the orbit and, subsequently, the worst-case scenario, the optimal magnitude computation has to be integrated within the min-max optimisation algorithm.

Algorithm 2 summarises the process: an outer loop computes the manoeuvre direction at constant magnitude; after computing the optimal direction, $\mathbf{d}_{opt}$, with Eq. 7, the new worst-case ellipse is computed; if $P_C < P_{C0}$ an inner loop

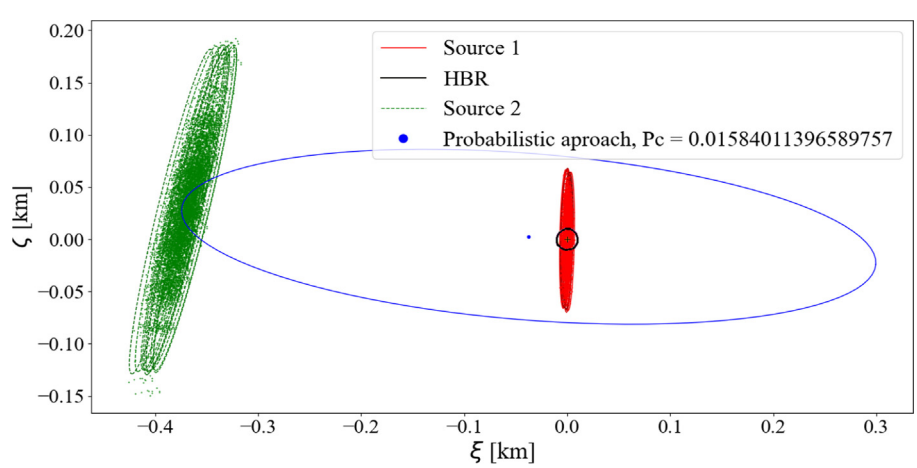

Fig. 2. Encounter geometry accounting for epistemic uncertainty under DSt. Two sources of information are considered. Aleatory and epistemic uncertainty is included. Source 1 (red) is nine times more reliable than Source 2 (green). The maximum and minimum PoC associated to each family of ellipses is: [0.3356, 0.3615] for Source 1 and [0.0, 2.1231e-256] for Source 2. The HBR, is shown in black, and equal to 5m. The uncertain ellipse combining information form both sources is shown in blue, with $P_C = 0.00158$.

reduces the magnitude of the impulse with a simple bisection method till $P_C = P_{C0}$, recalculating the worst-case ellipse at each iteration of the inner loop.

2.5. Optimisation of low-thrust collision avoidance manoeuvres under epistemic uncertainty

In this section, an approach to approximate the optimal manoeuvre using LT propulsion is presented. The process is divided in two steps. First, we define a low-thrust arc and take the middle point of the arc. At the middle point of the arc, θ_m, we use Algorithm 2 to compute an approximation of the direction of the thrust along the arc. We then apply the approximation to the thrust direction to the whole arc with constant thrust acceleration ε. (see Fig. 3).

With the arc length, arc angular position, thrust magnitude and direction of the manoeuvre, we use the analytical solution implemented in FABLE Di Carlo et al. (2018), Zuiani and Vasile (2014), to compute the effect of the manoeuvre on the impact plane. Given the direction and the magnitude of the thrust, FABLE computes the variation of the orbital elements along the thrust arc. The calculation is done in non-singular equinoctial elements $E = [a, P_1, P_2, Q_1, Q_2, L]$ Zuiani and Vasile (2014) by solving Gauss's planetary equations:

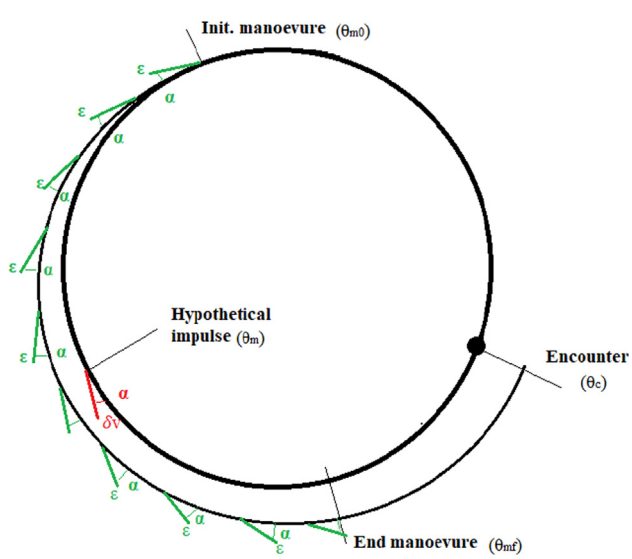

Fig. 3. CAM strategy for the LT scenario. The encounter occurs at θ_c. The manoeuvre is defined by the mid-point of the arc, θ_m. The arc-length is defined by the manoeuvre starting point, θ_{m0} and the final manoeuvre position, θ_{mf} so that: $\Delta\theta_m = \theta_{mf} - \theta_{m0}$, with $\theta_{mf} - \theta_m = \theta_m - \theta_{m0}$. The final manoeuvre position may or may not be equal to the encounter position, θ_c. The optimal manoeuvre direction in an object centred reference frame, α and β (for simplicity in the figure only one direction angle is shown), is computed at the mid-point position, θ_m, by obtaining the optimal impulse manoeuvre at this position, $\delta\mathbf{v}_{opt}$ (in red). A LT acceleration is performed from θ_{m0} to θ_{mf} with direction α (and β) and magnitude $\varepsilon = \min(\varepsilon_{max}, \delta v/\Delta t_b)$ (in green). The deflection $\delta\mathbf{x}_b$ can be computed as the difference between the original and the deflected orbits.

$$\frac{dE}{dL} = \varepsilon F(E, L, \alpha, \beta), \tag{11}$$

under the assumption that the thrust is small compared to the magnitude of the local gravity field. $L = \Omega + \omega + \theta$ is the true longitude, where θ is the true anomaly, ω the argument of the pericentre and Ω the right ascension of the ascending node. In Eq. 11 α and β are the LT direction angles in the <R,T,H> reference frame attached to the spacecraft so that the acceleration vector is defined as:

$$\begin{aligned} e_r &= \varepsilon \cos\beta \cos\alpha \\ e_t &= \varepsilon \cos\beta \sin\alpha \ , \\ e_h &= \varepsilon \sin\beta \end{aligned} \tag{12}$$

If E_0 is the set of orbital elements at the start of the thrust arc, an approximation of the value of the orbital elements at the end of the arc can be computed with the first order expansion:

$$E = E_0 + \varepsilon E_1 + O(\varepsilon^2) = \begin{bmatrix} a_0 + \varepsilon a_1 \\ P_{10} + \varepsilon P_{11} \\ P_{20} + \varepsilon P_{21} \\ Q_{10} + \varepsilon Q_{11} \\ Q_{20} + \varepsilon Q_{21} \end{bmatrix} + O(\varepsilon^2) \tag{13}$$

Substituting in Eq. 11 and taking only terms up to first order, it is possible to obtain:

$$\begin{aligned} &\tfrac{dE_0}{dL} = 0 \\ &\varepsilon \tfrac{dE_1}{dL} = \varepsilon F(E_0, L, \alpha, \beta) \end{aligned} \tag{14}$$

Thus, the first-order term of the expansion is:

$$E_1 = \int_{L_{m0}}^{L_{mf}} F(E_0, \mathscr{L}, \alpha, \beta)\, d\mathscr{L} \tag{15}$$

Once the new orbital elements at the end of the thrust arc are available, FABLE is used to propagate a coast arc ($\varepsilon = 0$) with the variated trajectory from the end of the manoeuvre to the nominal Time of Closest Approach (TCA) (where the impact plane is defined) under the simplifying assumption that the manoeuvre and orbit perturbation do not modify the shape of the ellipsoid of uncertainty (note that this is analogous to taking only the first two statistical moments in a full nonlinear propagation of uncertainty). Under this simplifying assumption the low-thrust manoeuvre, as the impulsive one, produces a translation of the uncertain ellipse on the impact plane by the quantity:

$$\delta x_b = r_{e_{LT}} - r_{e_0}. \tag{16}$$

Algorithm 3 summarises the LT CAM optimisation.

2.5.1. Magnitude and Arc-length optimisation

The previous section started from the assumption that one knows the magnitude of the thrust acceleration and the length of the thrust arc. In fact the optimal value of these two parameters is not known a priori. Thus we start

from a first guess and then follow an iterative process to find an optimal value.

Once the optimal direction, $\mathbf{d}_{opt}$, is available for a fixed magnitude and arc length, one can look for the optimal magnitude, the optimal arc length or both by iterating the following process:

- Keeping the thrust-arc length constant ($\Delta L = L_{mf} - L_{m0} = L_c - L_{m0}$), the acceleration magnitude is modified so that $P_C < P_{C0}$, and ε is minimal. Thus, similar to the impulsive case the magnitude is reduced till $P_C = P_{C0}$ and $\varepsilon > 0$. Algorithm 4 includes the pseudo-code of this optimisation.
- Keeping the acceleration magnitude and direction constant, the arc-length is reduced. In this case, we keep the mid-point of the arc fixed, and with a bisection method reduce the arc size until $P_C = P_{C0}$ and $\Delta\theta > 0$. Algorithm 5 summarises this optimisation.

Note that in the remainder of the paper we either optimise the magnitude or the arc-length. The simultaneous optimisation of both is of course possible but in this paper we limited our attention to the effect of each individual optimisation.

3. Intelligent classification system

In previous work by the authors, an ICS was introduced to support operators to make informed decisions on conjunction events Sánchez and Vasile (2021). The ICS was trained on thousands of conjunction scenarios in order to provide robust recommendations when a new scenario was occurring. However, the ICS was trained without taking into account the actual execution of a CAM. Thus in this section we assess the feasibility of including the cost of a CAM in the training of the ICS.

As in previous developments of the ICS, the intelligence comes from a combination of DSt, to establish the classes from the available information, and Machine Learning, to by-pass the computational burden required to compute Belief and Plausibility and aggregate other decision factors, like the TCA, for example, to return a class. From a methodological point of view, the ICS will be trained on a synthetic data-set containing a large variety of carefully constructed encounter scenarios and possible CAMs. Since the ICS is devised to provide support even in the case of events that fall outside the currently available record of conjunctions and collisions, it is of paramount importance that the ICS is trained on a carefully constructed database. For this reason, the data-set has to be composed of a sufficient variety of synthetic encounter geometries and associated uncertainties. Using existing data-sets of actual CDMs would not be sufficient or appropriate as it would introduce a potential bias. In fact, given the small number of catastrophic collisions, those events with a high P_C would not be adequately represented. It is also important to underline that the ICS is not devised to predict CDMs, or the uncertainty in CDMs, starting from raw data. On the contrary, the ICS is designed to provide a class given an available epistemic model. Thus the training of the ML model requires only a number of well thought geometries and a sufficiently large epistemic set but no real conjunction scenarios. Indeed, the training can be integrated with actual scenarios but paying attention to the balance of the data-set. In the remainder of this section we will briefly recall the two main components of the ICS: the classification system based on DSt and the Machine Learning model used to automate the classification.

3.1. Conjunction classification criteria

The Intelligent Classification System in Sánchez and Vasile (2021) was collecting conjunction events in 5 Classes and associated recommendations:

- Class 1: short-term high-risk encounter or short-term encounter with high degree of uncertainty. A CAM should be implemented.
- Class 2: mid-term or long-term high-risk encounter. A CAM should be considered, although more observations can be acquired before executing the CAM.
- Class 3: mid-term or long-term event affected by a high degree of uncertainty. More measurements have to be obtained before making any further decision.
- Class 4: mid-term or long-term low-risk event. No action is required, although more observations may be acquired to refine the position knowledge.
- Class 5: short-term low-risk encounter. No further action is required.

The allocation of a conjunction event to one of the above 5 classes was dependent on four main criteria: the Belief and Plausibility that the PoC, computed using the FE associated to the vector $\mathbf{u} = \left[\mu_\xi, \mu_\zeta, \sigma_\xi^2, \sigma_\zeta^2, \sigma_{\xi\zeta}\right]$, was above a given threshold P_{C0}, the Degree of Uncertainty $DoU|_{P_{C0}} = Pl|_{P_{C0}} - Bel|_{P_{C0}}$ on the PoC being greater than that threshold, the limit probability of collision P_{Cb} above which there is insufficient evidence supporting the correctness of the PoC, $Bel|_{P_C} < Bel_0$ for $P_C > P_{Cb}$, and the TCA. The TCA was used to divide conjunctions in three groups: short-term ($t_{TCA} < T_1$), mid-term ($T_1 \leqslant t_{TCA} < T_2$), and long-term($t_{TCA} \geqslant T_2$). The other criteria were used to further divide the events into the 5 classes defined above. Table 1 summarises the classification in Sánchez and Vasile (2021).

When the magnitude and effect of a CAM is available the classification can be modified to consider whether a manoeuvre can be executed or not and when. Classes 4 and 5 are not considering the possible execution of a manoeuvre, thus they are not affected by the information on the CAM. Class 1 recommends a CAM execution inde-

Table 1
Primary classification criteria.

Time to TCA	PoC for $Bel\|_{P_C} = Bel_0$	DoU at P_{C0}	Class
$t_{TCA} < T_1$	$P_{Cb} \geqslant P_{C0}$	-	1
	$P_{Cb} < P_{C0}$	$DoU\|_{P_{C0}} \leqslant \Delta$	5
		$DoU\|_{P_{C0}} > \Delta$	1
$T_1 \leqslant t_{TCA} t_{TCA} < T_2$	$P_{Cb} \geqslant P_{C0}$	-	2
	$P_{Cb} < P_{C0}$	$DoU\|_{P_{C0}} \leqslant \Delta$	5
		$DoU\|_{P_{C0}} > \Delta$	3
$T_2 \leqslant t_{TCA}$	$P_{Cb} \geqslant P_{C0}$	-	2
	$P_{Cb} < P_{C0}$	$DoU\|_{P_{C0}} \leqslant \Delta$	4
		$DoU\|_{P_{C0}} > \Delta$	3

pendently of the magnitude or position, and it will not be affected since already represents the highest degree of risk.

Once the CAM is computed Class 2 is reclassified to 1 if a CAM is below a given threshold at any orbital position prior to TCA, i.e. $\delta v < \delta v_0 \; \forall \; \theta_m \in \Theta_m$, where Θ_m is the set of angular positions where the robust optimal CAMs are computed. If the cost of the CAM is higher than the threshold δv_0 Class 2 remains unchanged but new measurements are recommended before recomputing the CAM.

Class 3 is reclassified as 1 or 2 depending on the magnitude of the CAM. When the CAM cost is above the threshold for any orbital position the event remains as Class 3, indicating more measurement are required to make a confident decision. However, if an earlier CAM is smaller than a later one, the event is reclassified as Class 1 and the optimal CAM and position provided. If the CAM is below the threshold for every orbital position, i.e. $\delta v < \delta v_0 \; \forall \; \theta_m \in \Theta_m$, the event is reclassified as Class 2: the low cost of the manoeuvre may justify its execution, but the higher degree of uncertainty and the fact that a later manoeuvre does not increase the cost supports the fact that acquiring more measurements can lead to a better decision. Table 2 summarises the reclassification proposed in this paper.

3.2. Machine learning-based classification

In Sánchez and Vasile (2021) the ICS was returning a Class and a recommended action given an input vector containing the TCA and the lower and upper bounds on miss distance and covariance matrix $\left(\left[\underline{\mu}_\xi, \underline{\mu}_\zeta, \underline{\sigma}^2_\xi, \underline{\sigma}^2_\zeta, \underline{\sigma}_{\xi\zeta}\right], \left[\overline{\mu}_\xi, \overline{\mu}_\zeta, \overline{\sigma}^2_\xi, \overline{\sigma}^2_\zeta, \overline{\sigma}_{\xi\zeta}\right]\right)$ for each source of information, thus, the length of the input vector was 12, times the number of sources plus one.

Table 2
New epistemic classification criterion.

Class in Table 1	δv criterion	New Class
Class 1	-	1
Class 2	$\delta v < \delta v_0 \; \forall \; \theta_m$	1
	else	2
Class 3	$\begin{cases} \delta v < \delta v_0 \text{for} \theta_m > \theta_{m0} \\ \delta v \geqslant \delta v_0 \text{for} \theta_m < \theta_{m0} \end{cases}$	1
	$\delta v < \delta v_0 \; \forall \; \theta_m$	2
	else	3
Class 4	-	4
Class 5	-	5

When CAMs are accounted for in the classification system, the ICS has to be retrained on the new Classes. The input to the ICS remains unchanged but the Classes are now the ones in Table 2. Thus, the ICS takes as inputs the time to the encounter, the bpas and the lower and upper bounds on mean and covariance components, and returns one of the Classes in Table 2.

In both the case of an impulsive and a low-thrust CAM, the ICS is trained by considering the equivalent δv. The value of the δv for impulsive manoeuvres comes directly from problem (9). In the case of a low-thrust manoeuvre one has the thrust magnitude ε and the length of the thrust arc Δt_b.

From these two quantities it is possible to compute the associated equivalent velocity change using: $\delta v = \varepsilon \Delta t_b$. Ultimately, the LT CAM using the process in Section 2.5 starts with an impulsive δv. Thus, the same classification criterion in Table 2 is used to classify both an event with an impulsive manoeuvre and one for a LT manoeuvre.

In this work, two different ML techniques have been tested: RF and ANN. We opted to use them and no others based on the results from previous works Sánchez and Vasile (2021). There, we tested a first version of the ICS over several databases representatives of different encounter geometries with four different ML techniques: Random Forests, Artificial Neural Networks, Support Vector Machines and K-Nearest Neighbours. The two first techniques provided the most accurate predictions over all the databases.

RFs were implemented using the available packages included in Python's Scikit library. The number of estimators and the depth of the trees were the main parameters modified during the training. ANN's were implemented with the Matlab's Deep Learning Toolbox. Only architectures with one hidden layer were considered. The number of neurons on this layer was the only tuned parameter. Information on the set of hyperparameters employed on this work are detailed in Section 4.4.2. More information on these techniques can be found in Breiman (2001) and Kubat (2017). It has to be noted that the scope of this paper is not to propose a particular ML architecture or to develop the best architecture to account for CAMs in the classification of conjunction events. The experiments in this paper are motivated by the successful classification of conjunction events, without CAMs, published in Sánchez and Vasile (2021). Thus in this paper we limited ourselves to the ML architectures used in Sánchez and Vasile (2021) and defer the analysis and development of more advanced ML models to future work.

4. Numerical experiments

In this section, we start by putting the robust CAM model to the test on different scenarios. Then the perfor-

mance of the ICS will be assessed together with its ability to produce robust recommendations.

4.1. Impulsive CAM: Minimisation of the PoC under aleatory uncertainty

In this example, a numerical case is presented to show the validity of the linear CAM model in Eq. 1. Only aleatory uncertainty is considered in this case, thus the computation of an optimal CAM reduces to problem Eq. 7 for a given covariance matrix. The magnitude of the impulse is kept constant and equal to $\delta v_0 = 10$ cm/s.

Table 3 includes the reference orbital parameters at the encounter time of both objects and the Keplerian elements covariance matrix, $\mathbf{D}$, for the piece of debris (the secondary object), assumed diagonal. The manoeuvrable object (the primary) is assumed to be perfectly known. The miss distance on the b-plane before the CAM is $\mathbf{r}_e = [-0.143, 0.0, 0.494]^T$ km, and the probability of collision before CAM execution is $P_C = 9.898 \cdot 10^{-6}$.

In order to validate the solution coming from the linear model in Eq. 6 a trivial grid search on the impulse angles ϕ, ψ (Eq. 2) was used to find a close to optimal pair of angles. For each pair, the PoC at the encounter due to the impulse was computed. For each θ_m, the optimal direction was chosen as the pair of angles providing the minimum probability of collision.

In Fig. 4, the components, in the the primary object's <T,N,H> reference frame, of the direction of the optimal impulse vector, $\delta\hat{\mathbf{v}}_{opt}$, applied to the primary object as a function of the angular distance between the manoeuvre and encounter positions, $\Delta\theta = \theta_c - \theta_m$, are shown. In black, the results provided by the linear model. In red the value from the grid search, at each manoeuvre position θ_m, that optimises the PoC. The figure shows the good agreement between both values for all the components, with only slightly greater differences for late manoeuvres (small $\Delta\theta$).

Table 4 includes the Root Mean Squared Error (RMSE) and the Maximum Absolute Error (MAE) of each component of $\delta\hat{\mathbf{v}}_{opt}$ computed with the linear model with respect to the grid search value.

Table 3
Primary and secondary's nominal Keplerian elements and secondary's diagonal covariance matrix terms at encounter time.

Variable	Units	Object 1	Object 2
Semi-major axis (a)	[km]	7006.794	6292.553
Eccentricity (ecc)	-	$5.5 \cdot 10^{-4}$	0.6684
Inclination (i)	[rad]	1.3321	2.0291
RAAN (Ω)	[rad]	0.1537	6.1208
Argument of perigee (ω)	[rad]	0.0571	3.4077
True anomaly (θ)	[rad]	5.8100	2.4224
σ_a^2	[km^2]	-	$1.54 \cdot 10^{-3}$
σ_{ecc}^2	-	-	$7.24 \cdot 10^{-9}$
σ_i^2	[rad^2]	-	$4.925 \cdot 10^{-7}$
σ_Ω^2	[rad^2]	-	0
σ_ω^2	[rad^2]	-	0
σ_θ^2	[rad^2]	-	0

4.2. Impulsive CAM: Minimisation of the PoC under epistemic uncertainty

In this section, we consider a scenario in which the miss distance and the covariance are affected by epistemic uncertainty. This can be the case in which multiple CDMs are in conflict or correspond to an unknown distribution of covariance matrices. In this scenario the CAM needs to be robust enough to cope with the distribution of the covariance matrices and optimal at the same time. We consider two cases: one with a non optimal impulse magnitude and one with an optimised magnitude.

Table 5 includes the exact orbital elements at initial time t_0 of both objects. The primary object, which is the manoeuvrable one, is assumed to be perfectly known. The knowledge of the orbit of the secondary object is affected by epistemic and aleatory uncertainty. Assuming Keplerian motion, the close approach occurs when the True Anomaly, $\theta = 0$ rad for both objects, and is set at one orbit and a quarter after t_0.

The uncertainty is introduced on the secondary object's initial position in its <T,N,H> reference frame. The aleatory uncertainty is modelled as a 3D-Gaussian distribution, with mean $\boldsymbol{\mu}_{tnh_0}$ and covariance matrix $\boldsymbol{\Sigma}_{tnh_0}$ (see Fig. 16a). The epistemic uncertainty is modelled with interval-valued parameters that modify the Gaussian distribution in Fig. 16b. Thus, the epistemic parameter $\boldsymbol{\lambda}_\mu$ defines the variability of the mean value, while the epistemic parameter $\boldsymbol{\lambda}_\sigma$, scales he covariance matrix. As a consequence, the single-well defined initial position uncertain ellipsoid becomes the family of ellipsoids:

$$\mathbf{x}_{tnh} = \mathcal{N}\left(\boldsymbol{\mu}_{tnh_0}, \boldsymbol{\Sigma}_{tnh_0}; \boldsymbol{\lambda}\right), \tag{17}$$

with $\boldsymbol{\lambda} = \left[\boldsymbol{\lambda}_\mu, \boldsymbol{\lambda}_\sigma\right]$ and

$$\boldsymbol{\mu}_{tnh} = \boldsymbol{\mu}_{tnh_0} + \boldsymbol{\lambda}_\mu$$

$$\boldsymbol{\Sigma}_{tnh} = \begin{bmatrix} \sigma_{t0}^2 \lambda_{\sigma_t} & 0 & 0 \\ 0 & \sigma_{n0}^2 \lambda_{\sigma_n} & 0 \\ 0 & 0 & \sigma_{h0}^2 \lambda_{\sigma_h} \end{bmatrix},$$

We also assumed that two independent sources of information were available. Each source of information was providing one interval for each of the epistemic parameters $\boldsymbol{\lambda}_\mu$ and $\boldsymbol{\lambda}_\sigma$. The intervals provided by each source were assumed to be completely disjoint and each epistemic parameter could belong to the interval provided by the corresponding source of information.

Table 6 includes the mean, $\boldsymbol{\mu}_{tnh_0}$ and covariance matrix, $\boldsymbol{\Sigma}_{tnh_0}$ for the secondary object's initial position modelling the aleatory uncertainty. It also includes the epistemic parameters that defined the family of ellipsoids for each source. The first source of information supports the hypothesis that the position is closer to the nominal mean

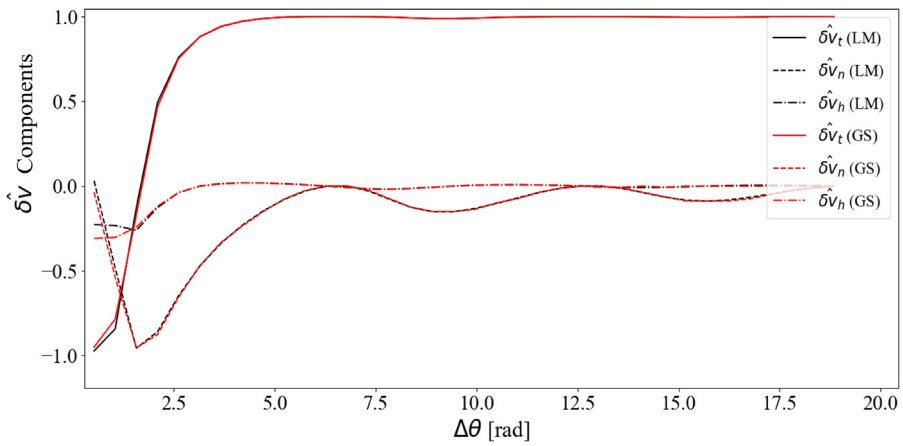

Fig. 4. Components of the unit vector $\delta\hat{\mathbf{v}}_{opt} = [\delta\hat{v}_t \;\; \delta\hat{v}_n \;\; \delta\hat{v}_h]$ parallel to the optimum impulse, $\delta\mathbf{v}_{opt}$, as a function of the angular difference between manoeuvre and encounter, $\Delta\theta = \theta_c - \theta_m$. Black: using Linear Model; red: grid search.

Table 4
Linear model errors with respect to the grid search value for the unit vector, $\delta\hat{\mathbf{v}}_{opt}$ parallel to the direction of the optimal impulse, $\delta\mathbf{v}_{opt}$.

Variable	RMSE	MAE
$\delta\hat{v}_t$	$5.434{\cdot}10^{-2}$	$5.792{\cdot}10^{-2}$
$\delta\hat{v}_n$	$4.244{\cdot}10^{-2}$	$5.512{\cdot}10^{-2}$
$\delta\hat{v}_h$	$2.619{\cdot}10^{-3}$	$7.039{\cdot}10^{-2}$

Table 5
Nominal Keplerian elements at initial time.

Variable	Units	Object 1	Object 2
Semi-major axis (a)	[km]	7100	7100.5
Eccentricity (ecc)	-	10^{-5}	10^{-5}
Inclination (i)	[rad]	$\pi/4$	$2/3\pi$
RAAN (Ω)	[rad]	0.0	0.0
Argument of perigee (ω)	[rad]	0.0	0.0
True anomaly (θ)	[rad]	4.7148	4.7148

Table 6
Secondary object's initial uncertainty. Aleatory uncertainty: nominal position, $\boldsymbol{\mu}_{tnh0}$, and diagonal covariance matrix, $\boldsymbol{\Sigma}_{tnh0}$, on its <T,N,H> reference frame. Epistemic uncertainty: two sources of information providing the interval-valued parameters, $\boldsymbol{\lambda}_\mu, \boldsymbol{\lambda}_\sigma$, that modify the mean and the covariance matrix elements.

Aleatory uncertainty			
$\boldsymbol{\mu}_{tnh0}$	[km]	[0, 0, 0]	
σ^2_{t0}	[km^2]	0.25^2	
σ^2_{n0}	[km^2]	0.25^2	
σ^2_{h0}	[km^2]	0.25^2	
Epistemic uncertainty		Source 1	Source 2
$\lambda_{\mu_t} = \lambda_{\mu_n} = \lambda_{\mu_h}$	[km]	[0.00, 0.01]	[-0.53, -0.515]
$\lambda_{\sigma_t} = \lambda_{\sigma_n} = \lambda_{\sigma_h}$		[1,4]	[1/5, 1/2]

(less than 10m off the nominal position) and is scaling the covariance matrices up to 4 times. The other source of information supports the hypothesis that the miss distance is further away (around 500m from the nominal position) and shrinks the covariance matrix by a factor between 2 and 5.

The uncertainty was expressed in an Earth Centred Inertial reference frame and propagated to the nominal encounter time. The propagation was carried out by sampling the initial ellipsoids defined by each source and propagating each sample to the nominal TCA. Finally, the uncertainty was projected onto the b-plane centred at the secondary object (see Section 2.1). Since we assumed independence of the sources the projection on the b-plane corresponds to two families of uncertain ellipses (see Fig. 5), defined by the intervals in Table 7. The PoC accounting for epistemic uncertainty varies then in the intervals $[10^{-21}, 9.1 \cdot 10^{-3}]$ and $[10^{-39},\ 1.5{\cdot}10^{-8}]$ for Source 1 and Source 2, respectively, when taken independently. If one was considering one single enveloping ellipsoid, assuming both sources equally reliable, the PoC would be $2.571 \cdot 10^{-5}$. When the intervals provided by the two sources are combined, the epistemic uncertainty space U is composed of 32 focal elements coming from the Cartesian product of two intervals for each of the 5 parameters defining the mean value and covariance matrix. The CAM has to be optimal for every value of mean and covariance in in each focal element.

In the following figures, the optimal impulse has been computed at each quarter of orbit for the 12 revolutions before the TCA. Fig. 6 shows the evolution of the components of the unit vector parallel to the optimal impulse, $\delta\hat{\mathbf{v}}$, as a function of the angular distance from the TCA, $\Delta\theta = \theta_c - \theta_m$, for both cases with and without optimisation of the impulse magnitude. For these examples, both strategies present the same optimal direction at all manoeuvre positions and it tends to a tangential impulse. They differ, however, in the value of the magnitude for $\Delta\theta > 56.5$ rad (approximately 9 orbits before TCA) when $P_{C_{WC}} < P_{C0}$ (Fig. 7), being WC the worst-case ellipse with highest PoC among all the FE.

Fig. 8 includes the evolution of the worst-case PoC as a function of $\Delta\theta$. It can be seen how the worst-case scenario PoC remains closer to P_{C0} by optimising the magnitude of the impulse for $\Delta\theta > 56.5$ rad (red solid line).

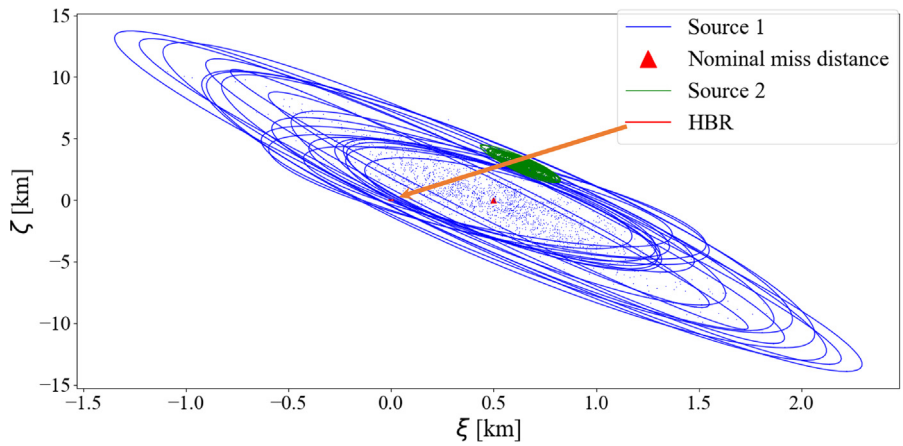

Fig. 5. Encounter geometry accounting for epistemic uncertainty in two families of ellipsoids from two independent sources of information: Source 1 in blue, Source 2 in green. The nominal miss distance is shown with a red triangle. The HBR, with solid red line (highlighted with an orange arrow to indicate its position in the origin of coordinates). The maximum and minimum PoC associated to each family of ellipses is: $[10^{-21}, 9.1 \cdot 10^{-3}]$ for Source 1 and $[10^{-39}, 1.5 \cdot 10^{-8}]$ for Source 2. The PoC corresponding to the probabilistic approach with a single bigger ellipse enclosing all the samples from both sources would be $2.571 \cdot 10^{-5}$.

Table 7
Bounds of the sources' intervals for the uncertain variables on the b-plane.

Variable	Units	Source 1	Source 2
μ_ξ	[km]	[0.406, 0.572,]	[0.338, 0.380]
μ_ζ	[km]	[-0.842, 0.625]	[2.708, 2.998]
σ^2_ξ	[km^2]	[0.0316, 0.312]	[0.931, 5.611]$\cdot 10^{-3}$
σ^2_ζ	[km^2]	[1.452, 20.12]	[0.3298, 0.0480]
$\sigma_{\xi\zeta}$	[km^2]	[0.180 , 2.422]$\cdot 10^{-2}$	[0.498, 3.962]$\cdot 10^{-2}$

Finally, Fig. 9 includes the worst-case scenario uncertain variables as a function of $\Delta\theta$ along with the sources' interval bounds. It can be appreciated how the worst-case scenario (blue and red solid lines for the non optimal magnitude and optimal magnitude cases, respectively) is restricted to the given intervals provided by the sources of information (black and green dashed lines).

The results of the optimisation using the linear model for computing the optimal impulse are compared with a Monte Carlo (MC) simulation in order to prove their validity. For the MC simulation, 1,000 samples per ellipsoid and 20 ellipsoids per source were used. The initial nominal state of the primary object (not uncertain) is propagated to the manoeuvre position where the optimal impulse is added to the orbital velocity. The new modified orbit is propagated to the unperturbed nominal TCA. The secondary object is propagated as indicated before: samples from a number of uncertain ellipsoids on the initial position are taken and individually propagated to the nominal TCA. The relative position between the primary nominal state and the state of each sample from the secondary object are propagated to the b-plane defined at the TCA by the unperturbed nominal orbits.

Fig. 10 shows the displacement of the set of ellipses obtained using the linear model (blue and green lines are associated to source 1 and source 2, respectively), and the uncertain ellipses families obtained with the MC simulation

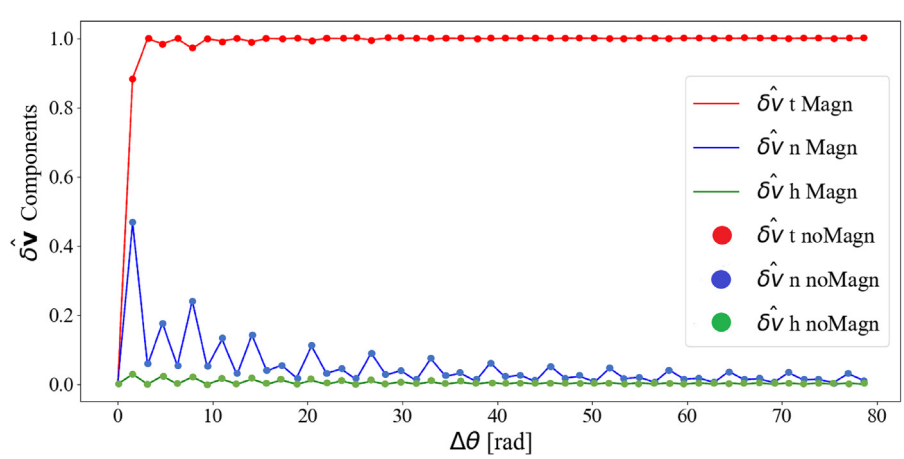

Fig. 6. Evolution of the direction of the optimal impulse, $\delta\hat{\mathbf{v}}$, as a function of the position of the manoeuvre, $\Delta\theta$: Solid line, with optimisation of the magnitude of the impulse, points, without optimisation of the magnitude. Both cases coincide. Red: tangential component, blue: normal component, green: out-of-plane component.

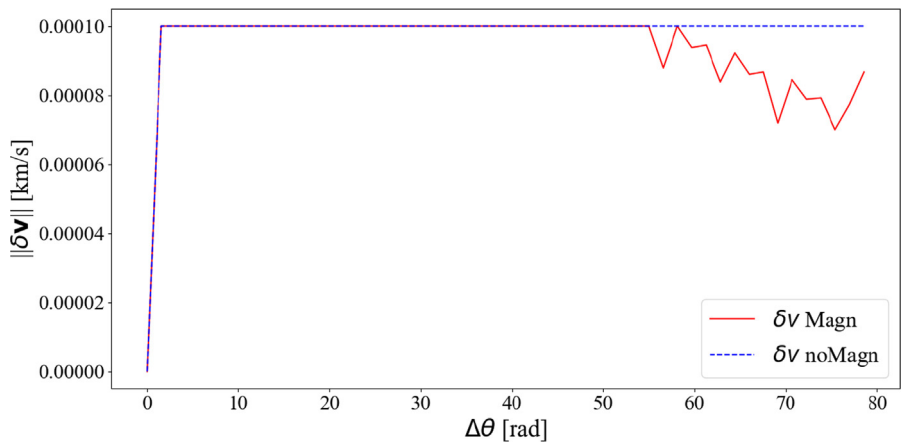

Fig. 7. Evolution of the impulse magnitude when optimised (solid red line) and without being optimised (dashed blue line) as a function of the position of the manoeuvre, $\Delta\theta$.

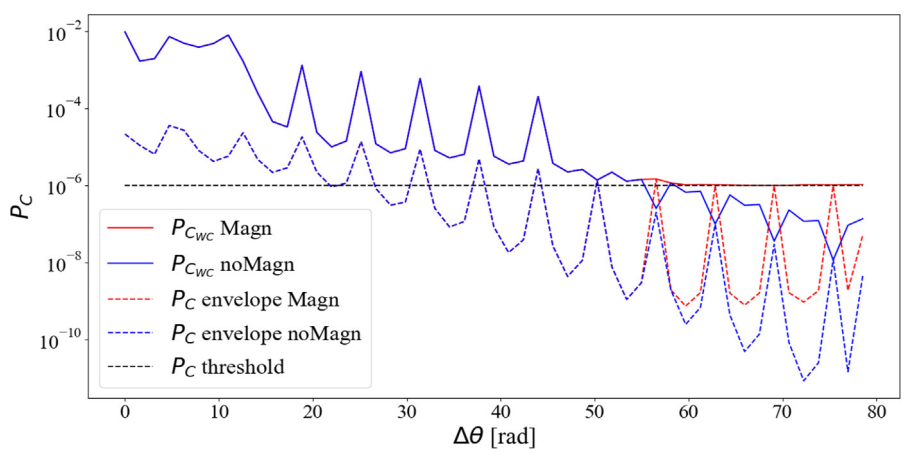

Fig. 8. Evolution of worst-case scenario PoC with the position of the manoeuvre, $\Delta\theta$. Red, with optimisation of impulse magnitude. Blue, without optimisation of impulse magnitude. Solid lines: worst-case scenario. Dashed lines: the worst-case PoC among the 20 ellipses per source randomly drawn from the intervals defined by the sources. Horizontal dashed-dotted black line, PoC threshold, $P_{C0} = 10^{-6}$, below which bring PoC.

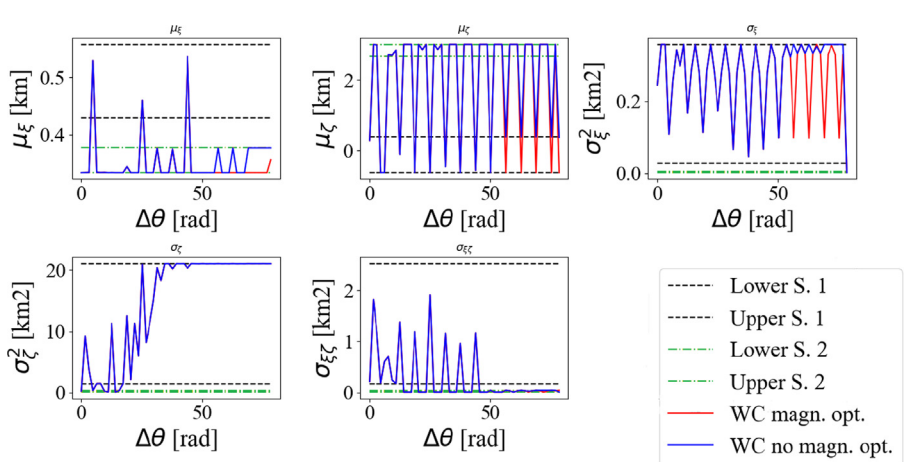

Fig. 9. Worst-case scenario uncertain variables evolution with respect to the difference between encounter and manoeuvre positions, $\Delta\theta$. From left to right and top to bottom: $\mu_\xi, \mu_\zeta, \sigma_\xi^2, \sigma_\zeta^2, \sigma_{\xi\zeta}$. Red solid line: with impulse magnitude optimisation. Blue solid line: without impulse magnitude optimisation. Black lines: Source 1's bounds (dashed lower, dashed-pointed upper). Green lines: Source 2's bounds (dashed lower, dashed-pointed upper).

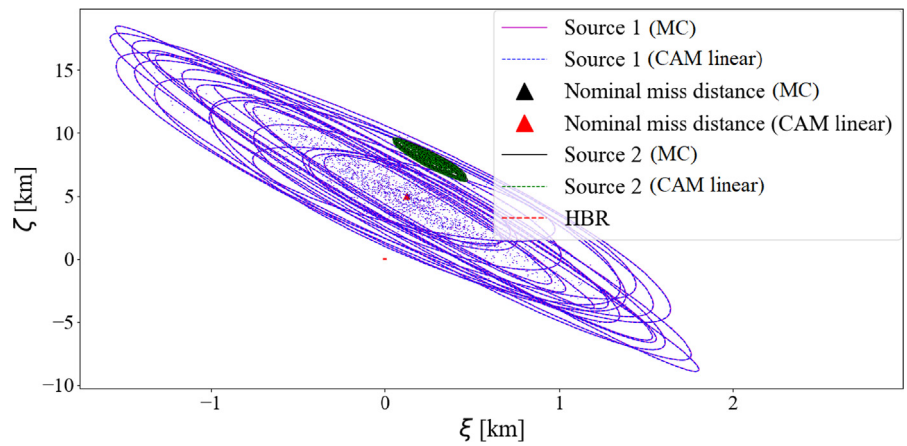

Fig. 10. Families of uncertain ellipses displaced by an optimal impulse applied at $\Delta\theta = 21.99$ rad (3.5 revolutions before the encounter). Blue and green dashed lines: uncertain ellipses displaced by the manoeuvre computed with the linear model. Purple and black solid lines: uncertain ellipses displaced with the MC simulation. Red dashed circle centred at the origin: HBR of the combined objects. Triangles represent the deflected mean relative position: red, displaced miss distance computed with the linear model; black, MC simulation.

(black and purple lines are associated to source 1 and source 2, respectively), when applying the optimal impulse 3.5 revolutions before the encounter. The figure shows a good agreement between the two simulations to the point that the purple and black lines are nearly completely overlapped to the blue and green ones. Fig. 11 illustrates the evolution of the deflection due to the impulse (Fig. 11a) and and the associated worst-case PoC (Fig. 11b) as a function of $\Delta\theta$. In red the MC simulation and with dots the linear model. The agreement between methods for all the variables can be understood as a validation of the linear model proposed on this work.

4.3. Low-thrust scenario

In this section, the performance of the method for computing the optimal CAM for the LT case is presented. We show a comparison between the different algorithms presented in Section 2.5. The results of each of these algorithms are then compared against the results obtained by applying a tangential manoeuvre, as proposed by other authors Hernando-Ayuso and Bombardelli (2020).

The same scenario as in the previous section is investigated. The exact orbital parameters are included in Table 5, the uncertainty in the initial position for the secondary object is included in Table 6 (the primary object is assumed to be perfectly known), and the encounter uncertain variables bounds according to the two sources of information are included in Table 7. The parameters employed for the LT scenario appear in Table 8. The optimal direction has been computed at multiples of half orbit before the encounter for 10 revolutions.

In Figs. 12–15, *Strategy 0* refers to the LT manoeuvre obtained using Algorithm 3 with $\varepsilon_{opt} = \varepsilon_{max}$ and with $\theta_{mf} = \theta_c$, thus, maximum thruster capacity and maximum arc-length. *Strategy 1* refers to the case where the accelera-

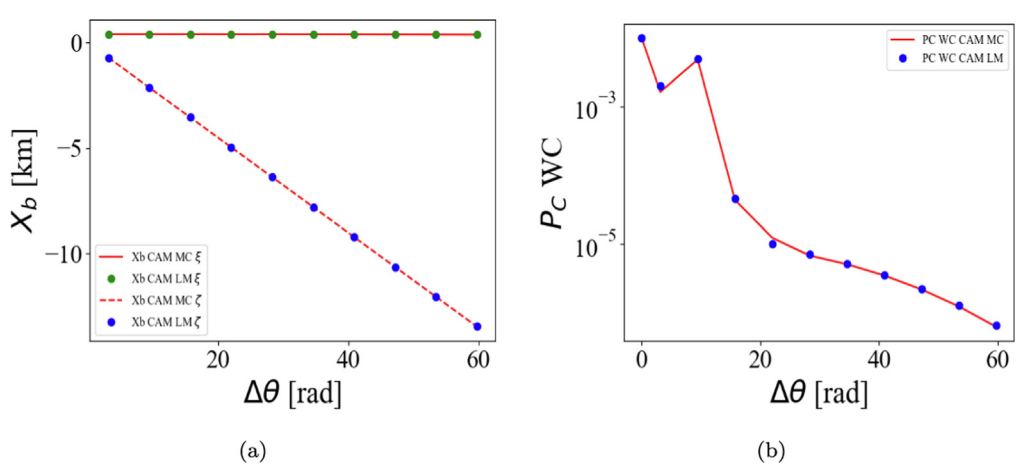

Fig. 11. (a) Evolution of the deflection due to the manoeuvre. Solid red line: ξ component MC simulation, dashed red line: ζ components MC simulation. Green dots: ξ component linear model. Blue dots: ζ component linear model. (b) Evolution of the PoC due to the manoeuvre. Solid red line: MC simulation. Blue dots: linear model.

Table 8
Parameters employed for the optimal LT CAM computation.

Variable	Units	Value
δv_{max}	cm/s	10
ε_{max}	cm/s^2	$2{\cdot}10^{-3}$
P_{C0}	-	10^{-6}

tion magnitude is optimised, keeping the thrust until the encounter. *Strategy 2* shows the case where the thrust is kept equal to the maximum capacity of the thruster and the arc-length is optimised. In Figs. 12–15, a comparison between the results obtained applied the LT in the optimal impulsive direction (solid lines) and the results obtained with a purely tangential thrust (dashed lines) is also presented.

Fig. 12 includes the evolution of the PoC as a function of the difference between the true anomalies at the manoeuvre mid-point and at the encounter, $\Delta\theta$. It can be seen the difference between executing the manoeuvre with maximum capacity until the encounter (blue solid line) and optimising the acceleration magnitude (red solid line) or the burning time (green solid line). For values $\Delta\theta > 30$ rad, if using the maximum capacity and maximum burning time, the PoC drops far below the threshold, P_{C0}. However, for the other two cases, the PoC remains close, but below the threshold. In Figs. 13 and 14, it can be seen how the acceleration magnitude and the burning time are optimised, respectively. Fig. 13 shows that for *Strategy 0* and *Strategy 2* the acceleration magnitude is equal to the maximum capacity, $\varepsilon = \varepsilon_{max}$, but for *Strategy 1* the acceleration is optimised (red solid line). Similarly, Fig. 14 illustrates the optimisation on the burning time for *Strategy 2* (green solid line), while *Strategy 0* and *Strategy 1* present the maximum burning-time. Finally, in Fig. 15, the equivalent velocity change obtained with the LT manoeuvre, according to $\delta v = \varepsilon/\Delta t_b$, for each strategy is shown. In general, it is different than the velocity change considered by the impulse employed to compute the optimal direction manoeuvre, which is shown as the horizontal black dashed line.

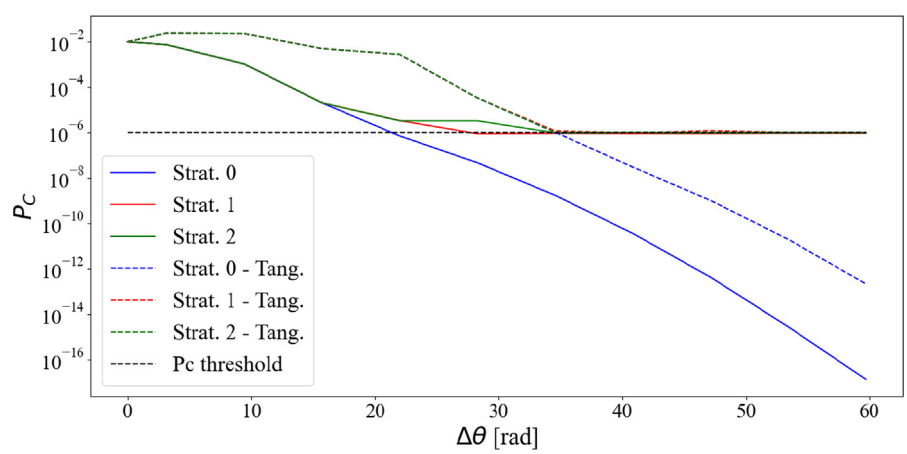

Fig. 12. PoC evolution with respect the difference in True Anomaly between the mid-point of the LT manoeuvre and the encounter ($\Delta\theta = \theta_c - \theta_m$). Blue: maximum thruster capacity and arc-length. Red: maximum arc-length and optimised accelerations magnitude. Green: maximum thruster capacity and optimised arc-length. Solid lines: direction of the impulse according to proposed algorithm. Dashed line: tangential manoeuvre.

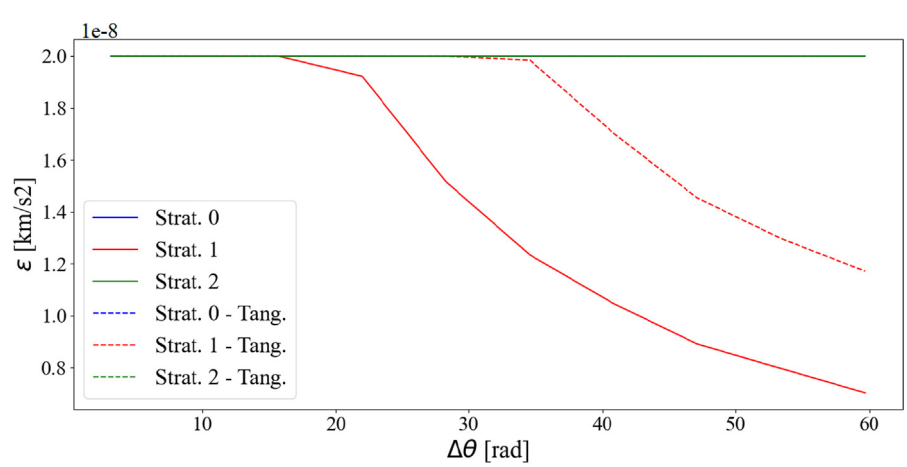

Fig. 13. Acceleration magnitude evolution with respect the difference in True Anomaly between the mid-point of the LT manoeuvre and the encounter ($\Delta\theta = \theta_c - \theta_m$). Blue: maximum thruster capacity and arc-length. Red: maximum arc-length and optimised accelerations magnitude. Green: maximum thruster capacity and optimised arc-length. Solid lines: direction of the impulse according to proposed algorithm. Dashed line: tangential manoeuvre.

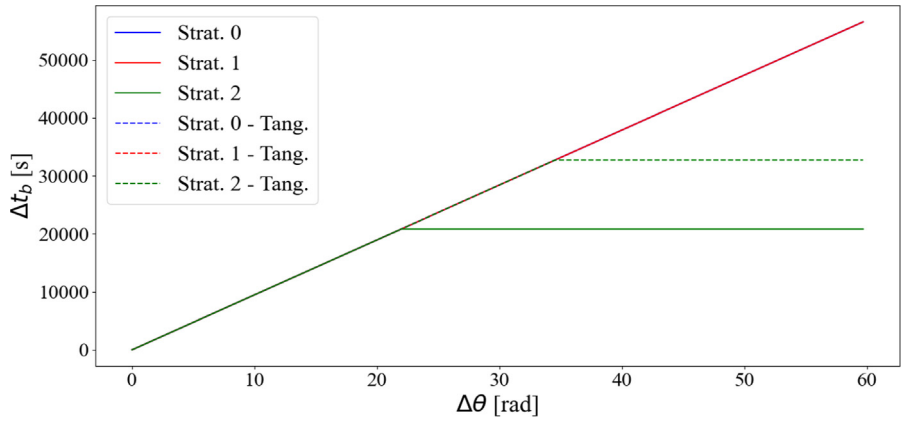

Fig. 14. Burning time evolution with respect the difference in True Anomaly between the mid-point of the LT manoeuvre and the encounter ($\Delta\theta = \theta_c - \theta_m$). Blue: maximum thruster capacity and arc-length. Red: maximum arc-length and optimised accelerations magnitude. Green: maximum thruster capacity and optimised arc-length. Solid lines: direction of the impulse according to proposed algorithm. Dashed line: tangential manoeuvre.

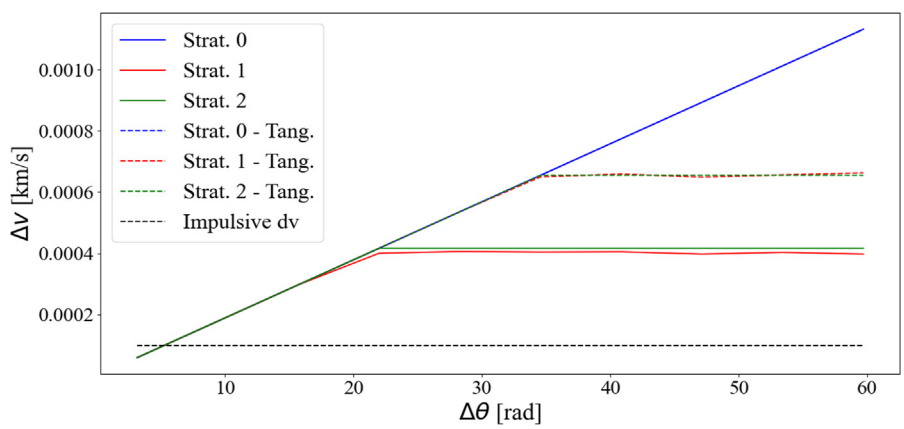

Fig. 15. Equivalent velocity change with respect the difference in True Anomaly between the mid-point of the LT manoeuvre and the encounter ($\Delta\theta = \theta_c - \theta_m$). Blue: maximum thruster capacity and arc-length. Red: maximum arc-length and optimised accelerations magnitude. Green: maximum thruster capacity and optimised arc-length. Black dashed line: velocity change used on the hypothetical impulsive manoeuvre. Solid lines: direction of the impulse according to proposed algorithm. Solid lines: direction of the impulse according to proposed algorithm. Dashed line: tangential manoeuvre.

When comparing with the tangential control law, it can be seen from Fig. 12 that, for all the approaches, the proposed method (solid line) yields a lower worst-case PoC than the tangential manoeuvre (dashed line) at any given value of $\Delta\theta$. This implies the proposed method improves over a purely tangential manoeuvre.

4.4. Intelligent classification system performance

This section presents the performance of the machine learning part of the proposed Intelligence Classification System when the execution of the manoeuvre is included in the decision process. The performance, understood as the capacity of the system to predict the correct Class, is measured with the overall accuracy of the ML model and the associated F1-score.

4.4.1. Definition of the data set

As explained in Section 3 the ICS needs to be trained on a carefully constructed database with a variety of encounter geometries and an inclusive uncertainty set. In order to test the methodology proposed in this paper, we created a synthetic database of close encounters between simulated space objects in Low Earth Orbit whose orbit and associated covariances (or set of CDMs) are assumed to be provided by two sources. The database contains the following features: the time to the TCA, the upper and lower bounds of the five uncertain variables, $\left[\mu_\xi, \mu_\zeta, \sigma_\xi^2, \sigma_\zeta^2, \sigma_{\xi\zeta}\right]$, provided by each of the two sources of information, the bpa of the source, and the set of positions (measured as the difference in true anomaly between execution and encounter positions) where the optimal CAM is computed along with the value of the manoeuvre at those positions (expressed in <T,N,H> reference frame). Finally, the Class of the event according to the new classification criterion in Table 2 is also included.

The close encounters were obtained by propagating an uncertain initial state from an initial position (i.e. the position at the last observation) to the nominal TCA. One of the objects is assumed to be perfectly known and manoeu-

vrable (i.e. an operational satellite), while the other is affected by uncertainty on the position and has no manoeuvre capabilities (i.e. piece of space debris). The close encounters are defined using the exact nominal orbital parameters. The values of the nominal initial Keplerian parameters of the primary object were sampled from the intervals defined in the upper part of Table 9. The nominal initial state of the secondary object was obtained by propagating backwards from the encounter the nominal state, obtained from the nominal encounter geometry. This nominal encounter geometry was defined by taking values from the intervals defined in the lower part of Table 9, where, following the procedure in Bombardelli and Hernando-Ayuso (2015), $\mathbf{r}_e$ is the miss distance, χ the ratio between secondary's and primary's speeds, ϕ the angle between both velocities within the primary's orbital plane and ψ the out-of-plane angle.

The uncertainty is included in the secondary object's initial position as explained in Section 4.2 (Figs. 16a and b). Then, the initial uncertainty position can be defined as:

$$\mathbf{x}_{tnh}^{(2)} = \mathcal{N}\left(0, \mathbf{\Sigma}_{tnh_0}; \boldsymbol{\lambda}\right). \tag{18}$$

The uncertainty is then propagated to the nominal TCA and projected on the nominal impact plane. The intervals for the encounter uncertain variables can be then obtained. Note that also in this case we use the simplifying and conservative assumption that the intervals for the miss distance and covariance associated to the propagated ellipsoids can be computed independently.

The data-set was generated considering two sources of information and the associated epistemic uncertainty intervals, on miss distance and the covariance matrix, were chosen so that the events could be grouped according to five families of encounter geometries. Sources were then fused as in Sánchez and Vasile (2021). These families are defined by the relative position of the two sources' sets of uncertain ellipses on the impact plane and the relative position between them and the HBR. These configurations represent different degrees of risk and conflict between sources: i) the two sets of ellipses overlaps between each other and with the HBR (high risk and low conflict), ii) the two sets overlaps between each other but not with the HBR (low risk and low conflict), iii) the sets do not overlap with each other and only one overlaps with the HBR (high conflict), iv) no overlapping between sets or with the HBR (low risk and high conflict), v) similar to the previous case, but with an hypothetical uncertain ellipse accounting for two sources set overlapping the HBR (low risk and low conflict).

Table 9
Intervals from which the primary object's nominal initial Keplerian elements and the nominal encounter geometry variables were obtained.

Value	Units	Parameter
a	[km]	[7000,7100]
ecc. (e)	-	$[10^{-5}, 10^{-4}]$
inc. (i)	[deg]	[70,90]
RAAN (Ω)	[deg]	[0,20]
Arg. Per. (ω)	[deg]	[0,20]
True An. (θ)	[deg]	[0,360]
$r_{e\xi}$	[m]	[-5,5]
$r_{e\eta}$	[m]	[-5,5]
$r_{e\zeta}$	[m]	[-5,5]
χ	-	[0.9,1.1]
ψ	[deg]	[-90,90]
ϕ	[deg]	[0,90]

The samples for each geometry were obtained as follows. The aleatory component of the uncertainty was modelled in the same fashion for all the sets of geometries. The mean of the initial position of the secondary object was set to zero for all the samples, $\boldsymbol{\mu}_{tnh_0} = [0, 0, 0]$ km. The three diagonal terms, $\sigma_{t0}^2, \sigma_{n0}^2, \sigma_{h0}^2$, of the aleatory component of the covariance matrix, $\mathbf{\Sigma}_{tnh_0}$, were drawn from the intervals [0.05,0.1], [0.01,0.1], [0.01,0.1] km^2, respectively. The epistemic component was obtained, for each geometry family, by sampling from the intervals included in Table 10. The samples were then propagated to the impact plane.

Finally, the optimal CAM (assumed impulsive) was computed at five positions: $\Theta_m = \{0.5, 1.5, 2.5, 5.5, 9.5\}$ revolutions before the TCA. The linear model detailed in Section 2 was employed to compute the optimal value. These five angular positions were used to classify the events according to the new classification criterion introduced in Section 3.1. Table 11 includes the parameters employed to create the database. The HBR was kept constant for all the virtual encounters. Likewise the threshold in PoC, Belief and Degree of Uncertainty (P_{C0}, Bel_0 and Δ, respectively) were kept constant for all encounters. Two time thresholds were considered, $T_2 > T_1$. The robust optimal CAM for each encounter was computed at the five positions included in Θ_m, measured as the angular distance between the manoeuvre position and the encounter position in True Anomaly. The CAM magnitude was optimised so that the risk of the worst-case scenario remained just below the PoC threshold, with a maximum capacity of the thruster of δv_{max}.

We initially considered a total of 18,000 simulated encounters, 3,600 for each of the five sets of geometries. Each group of 3,600 encounters were evenly distributed over the three time bins used in the classification: short-term, mid-term and long-term. For each time bin and each encounter configuration, one third of the PoCs was computed using two equally reliable sources of information, one third using two sources where one is nine times more reliable than the other, and one third where the same source is nine times less reliable than the other. We then applied the classification criteria in Table 2. The result can be seen in Fig. 17 where the database classified without accounting for the execution of the manoeuvre, Fig. 17a, is compared to the same database classified including the CAM, Fig. 17b.

From the figure, it can be seen that Classes 2 and 3 are underrepresented. This is mainly due to the fact that the

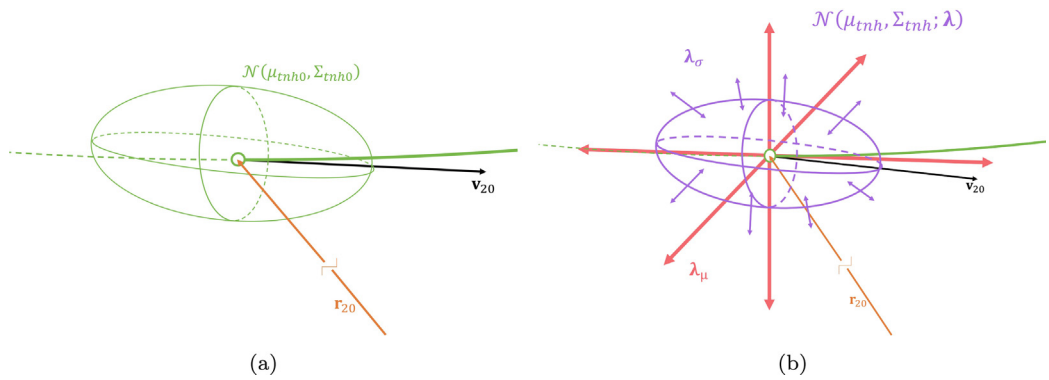

Fig. 16. (a) Aleatory uncertainty on the initial secondary position. Orange: initial nominal position ($\mathbf{r}_{20}$), black: initial nominal velocity ($\mathbf{v}_{20}$), green: aleatory uncertainty modelled as a Normal distribution, $\mathcal{N}(\boldsymbol{\mu}_{tnh0}, \boldsymbol{\Sigma}_{tnh0})$. (b) Epistemic uncertainty on the initial secondary position. Red: displacement on initial mean position, $\boldsymbol{\lambda}_\mu$, purple: scaling on the initial covariance matrix, $\boldsymbol{\lambda}_\sigma$. The total uncertainty follows a parametric family of Gaussian distributions: $\mathcal{N}(\boldsymbol{\mu}_{tnh0}, \boldsymbol{\Sigma}_{tnh0}; \boldsymbol{\lambda})$.

Table 10
Intervals from which the bounds of the epistemic parameters $\boldsymbol{\lambda}_\mu$ and $\boldsymbol{\lambda}_\sigma$, per each geometry configuration were obtained. The upper and lower bounds of $\boldsymbol{\lambda}_\mu$ and $\boldsymbol{\lambda}_\sigma$ are taken randomly from $\boldsymbol{\Lambda}_\mu$ and $\boldsymbol{\Lambda}_\sigma$, so that $\boldsymbol{\lambda}_\mu \in \boldsymbol{\Lambda}_\mu$ and $\boldsymbol{\lambda}_\sigma \in \boldsymbol{\Lambda}_\sigma$.

Geometry	Parameter	Source 1	Source 2
Geo. 1	Λ_μ [km]	[-0.01, 0.01]	[-0.01, 0.01]
	Λ_σ	[0.1, 0.4]	[0.1, 0.4]
Geo. 2	Λ_μ [km]	[0.35, 0.45]	[0.35, 0.45]
	Λ_σ	[0.5, 2]	[0.5, 2]
Geo. 3	Λ_μ [km]	[-0.01, 0.01]	[0.35, 0.45]
	Λ_σ	[0.1, 0.4]	[0.5, 2]
Geo. 4	Λ_μ [km]	[-0.1, -0.05]	[0.18, 0.23]
	Λ_σ	[0.1, 0.4]	[0.1, 0.4]
Geo. 5	Λ_μ [km]	[-0.15, -0.1]	[0.1, 0.15]
	Λ_σ	[0.1, 0.4]	[0.1, 0.4]

Table 11
Parameters employed to obtain the database.

Parameter	Units	Value
HBR	m	10
P_{C0}	-	10^{-6}
Bel_0	-	0.5
Δ	-	0.3
T_1	days	2
T_2	days	4
δv_{max}	cm/s	10
Θ_m	rad	$[\pi, 3\pi, 5\pi, 11\pi, 19\pi]$

magnitude of the manoeuvre tends to classify Class 2 and 3 geometries as Class 1. Due to this unbalanced Class distribution, the average performance of the ICS system was negatively affected, with a limited ability to correctly predict Class 2 and 3 scenarios. From different tests using more balanced databases, we observed that a less populated but more balanced database provided better prediction capabilities. Thus a new database which contained 174 samples per Class (870 in total) was created for the training of the ICS.

The features of the database are: time to TCA, sources' bpa, and the upper and lower bounds of the uncertain variables. The label of the database was the Class of the events. The database was split into two sets: 80% of the data points formed the Training set and 20% of data points were used as Validation set. The Training Set was used to train each model. The Validation Set was used to evaluate the performance of the trained models during the hyperparameter tuning (see next section). Note that the data in the Validation Set are not seen by the models during the training process but are used only to assess the performance of each model for a given combination of the hyperparameters.

4.4.2. Hyper-parameter setting

In this work, a few different RFs configurations were trained and tested. The models differed in the number of trees in the forest, *n_estimators*, (50, 100, 200, 400), the maximum depth of the tree, *max_depth*, ('None', 50, 100), the minimum number of samples required to be at a leaf node, *min_samples_leaf*, $(1, 10^{-4}, 10^{-7})$, the minimum number of samples to split a node ,*min_samples_split*, $(2, 20)$, and the number of features to consider when looking for the best split,*max_features*, ('auto',0.5,'log2'). For each combination of hyper-parameters, an RF model was re-trained using the Training Set and then tested on the Validation Set. The model with the combination of hyperparameters that provided the best results (the highest mean F1-score) over the Validation Set was saved as the best model.

The ANN's trained in this paper contain only one hidden layer. Since it is a classification problem, the output layer contains five nodes, one per Class, indicating the probability of the output of being one of them. The final output corresponds to the Class presenting a higher probability. Ideally, when inputs of a Class k are provided, all nodes in the output layer should take value 0 but node k that should take value 1. The only hyperparameter modified in this study was the number of neurons in the hidden layer: 10, 20, 50, 100. Each neuron possess a hyperbolic tangent activation function. The optimiser is based on the Levenberg-Marquardt method and the loss function is the Multi-Class Cross-Entropy. For each number of neu-

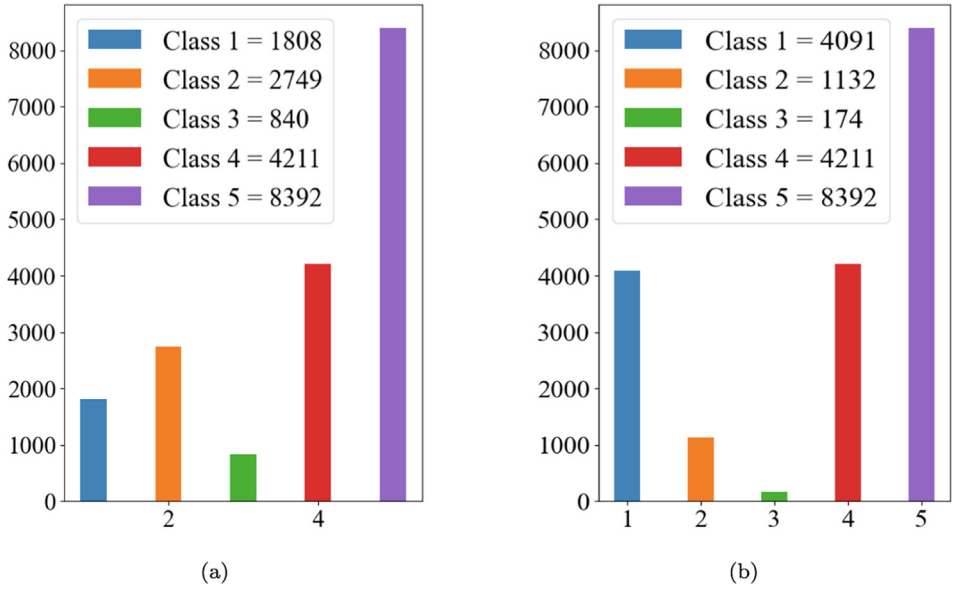

Fig. 17. Histograms representing the samples distribution by Classes: (a) unbalanced database with criterion presented in Sánchez and Vasile (2021), (b) unbalanced database with criterion in Table 2.

rons an ANN's model was trained iteratively 10 times with different initialisation of the parameters (weights and bias of the neurons) on the Training Set and then tested on the Validation Set. The ANN model providing the best value of the loss function on the Validation Set was selected as the best model.

4.4.3. Performance

The performance of each technique (RF or ANN) was obtained by predicting the results of the samples in the Validation Set. The metrics employed to assess the models are: the overall accuracy (the percentage of samples correctly predicted over all the samples), the precision by Class (the fraction of samples correctly predicted among the total number of samples predicted in that Class), the recall by Class (the fraction of samples correctly predicted in one Class over the total number of samples actually belonging to that Class), and the F1-score by Class and the mean F1-score among categories:

$$F_1 = 2\frac{recall * precision}{recall + precision}. \tag{19}$$

Table 12 shows the performance of the system using RF and ANN over the Validation Set of the balanced database. It can be seen that RF outperforms ANN, both in mean F1-score and on almost all individual Class F1-score. Overall, the performance of the system is good, a mean F1-score near 90%. Breaking down by Classes, it is worth noting how Classes 4 and 5 are almost perfectly predicted, while Class 3 presents the worst prediction score. The reason for a lower score, in this Class, is the lack if direct information on the magnitude of the manoeuvre. In fact the CAM itself is not an input and the ICS has to assume the presence of the CAM from the allocated class. Since Class 3 is the more ambiguous one, events are miss-classified as 1 or 2. Note also the low recall of Class 1, and the corresponding low precision of Class 2. This suggests that the ICS tends to generate a number of false Class 1 negatives that would induce the operator to acquire additional information before executing a CAM. Although the situation might improve with an extended database, this result is still positive, as it is, because it leads to the acquisition of more information. Indeed since Class 1 usually corresponds to short TCAs, the operator can anyway decide to implement a manoeuvre if there is no time to allocate a new observation.

From these results, it can be concluded that the system is able to predict, with a reasonable level of accuracy, the correct Class of a close encounter event, with the exception of Class 3. However, Class 3 is characterised by a medium-to-long term event and further decisions can be made. Furthermore, an event Class 3, with the added δv criterion, is miss-classified as more stringent Class 1 and 2. It can also be concluded that, out of the two ML algorithms we tested, RFs worked better for this problem.

As it will be shown in the next section, the classification errors are compensated by a significantly lower computational time compared to the exact calculation of Belief and Plausibility. When the number of uncertain intervals and dimensions increases the direct computation of Belief and Plausibility would make the screening of the whole catalogue of resident objects quite time consuming. Furthermore, all incorrect classifications would lead the operators to take the robust decision to prepare a CAM and acquire more information unless the available time is too short. What remains to be tested is the potential increase in unnecessary CAMs due to false positives. However, this can be done after operational constraints, on the execution of the CAM, are accounted for in the decision. This will be the subject of future work.

Table 12
Performance of the best models for predicting the close event Class.

Technique	Class	Accuracy	Precision	Recall	F1
RF	**Overall**	**90.33**	-	-	**88.03**
	1	-	**92.34**	**76.47**	**83.66**
	2	-	**77.54**	**94.04**	**85.0**
	3	-	**83.87**	**70.27**	**76.47**
	4	-	**98.67**	**98.23**	**98.44**
	5	-	**97.69**	**95.46**	**96.58**
ANN	Overall	87.67	-	-	82.05
	1	-	88.94	80.09	84.28
	2	-	75.56	86.81	80.79
	3	-	60.0	48.65	53.73
	4	-	96.01	96.02	96.01
	5	-	96.76	94.14	95.43

Table 13
Comparison on computational time for the risk assessment: using the ICS (left) against computing the actual values of the variables involved on the criterion (right). The time is given in seconds.

Prediction with ICS		Computing actual values	
Time ML	0.1875	Time Pl/Bel	29.7916
		Time CAM at Θ_m	93.7321
		Time criterion	1.5798
Total time	**0.1875**	Total time	125.1035

4.4.4. Computational time

In this section we compare the computational time required to the ICS to indicate the Class of an event and suggest an action against the computational time required to generate the same output but without ML. We use the same example as in Section 4.2. The bounds of the uncertain variables on the impact plane are included in Table 7, both sources are assumed to be equally reliable ($bpa_1 = bpa_2 = 0.5$) and the time to the nominal TCA is 2.0673 hours. This information represents the input to the ICS. With these values, the ICS indicates that the event has to be classified as Class 1: a CAM should be implemented. Table 13 shows the computation time required to evaluate the risk and classify the event. It can be seen that the use of the ML model in the ICS leads to a reduction of the computation time by three orders of magnitude. Note that these times refer to a case with 2 sources of information. If more sources of information were available the *Time Pl/Bel* would have increased, or if more positions had been included in Θ_m, *Time CAM*, the calculation of CAM, would have also been greater. This demonstrates the utility of the ICS at processing a potentially large number of events.

5. Conclusions

This paper has introduced an Intelligent Classification System to automatically make decisions on close encounter events and automatically allocate optimal CAMs. The system combines DSt to classify conjunction events under epistemic uncertainty with a ML model.

The system proposed in this paper has the distinctive property of accounting for epistemic uncertainty and multiple sources of uncertain information. The work in this paper demonstrated the use of DSt to compute robust estimates of the correctness of the PoC and generate robust CAMs. The paper provides a validation of the linear model used to compute both impulsive and low-thrust manoeuvres and of their robustness against both aleatory and epistemic uncertainty in the PoC.

The paper also demonstrated that the robust strategy to optimise low-thrust manoeuvres provides better results (lower propellant consumption) than the simple application of a tangential thrust.

On the data-set used in this paper, the RF classifier was shown to be able to reliably return the Class of the events and provide robust decisions on the execution of a CAM for most of the classes except for class 3, the one containing the most ambiguous cases. However, it was found that the miss-classification leads to the association of events to more conservative classes. It was also found that the low recall on Class 1 is due to the miss-classification of events as Class 2. Although this would lead to a less conservative decision still it would require to plan a CAM and assess its necessity.

It was also shown how the ICS provides a response order of magnitude faster than the actual calculation of the probability of collision, reliably bypassing *Pl* and *Bel* time-consuming computations. This result demonstrates the utility of the combination of the ML and DSt to provide a robust automation of space traffic management. As mentioned during the analysis of the results, the combination of ML and DSt provides very good prediction accuracy when the CAM magnitude is not considered to reclassify the events, while this accuracy is reduced once it is considered. This suggests either a different approach where the influence of the CAM magnitude is considered after the ICS step, or an improvement on the ML model. The former option would provide more flexibility but would also add computational cost as manoeuvres would need to be recomputed to evaluate every decision, unless a separate ML model was trained to predict the manoeuvre. The analytical model is sufficiently fast to allow this frequent recomputation but the solution of the robust optimisation

problem introduces a relatively high computational overhead. On the other hand more stringent operational constraints might need to be considered before even computing a CAM. Thus the need to compute a CAM could result to be limited to a small number of cases.

Since we considered only a limited number of ML algorithms, more work is required to find or develop a more specific ML model. Future work will look into a further extension of the calculation of the probability of collision accounting for the full probability distribution and the inclusion of constraints in the ICS. Finally, the epistemic uncertainty associated to the ML model itself was not considered in this work. The quantification of this additional source of uncertainty would improve the classification and the robustness of the decision. This source of uncertainty, along with a more detailed modelling of other sources of epistemic uncertainty will be considered in further works.

Declaration of Competing Interest

The authors declare the following financial interests/personal relationships which may be considered as potential competing interests: [Massimiliano Vasile reports financial support was provided by the European Space Agency].

Acknowledgment

This work was funded by the European Space Agency, through the "Idea I-2019-01650: Artificial Intelligence for Space Traffic Management".

Appendix A. Min-max optimisation algorithms

Min-max impulsive optimisation algorithm

Algorithm 1: Min-max impulsive CAM optimisation algorithm, assuming constant magnitude.

Initialise $\epsilon_{Pc}, \Delta P_C, \delta v_{max}$
$\mathbf{S} = []$
for $fe \in FE$ **do**
  $\mathbf{u}_{fe} = \arg\max_{\mathbf{u}\in\Omega_{fe}}(P_C)$
  $\mathbf{S} = \mathbf{S} + \mathbf{\Sigma}_{fe}$
end
Compute P_{C_1} with Eq. (4)
while $\Delta P_C > \epsilon_{Pc}$ **do**
  $\mathcal{T} = \mathbf{QT}^T\mathbf{S}^{-1}\mathbf{TQ}$
  Compute $\delta\mathbf{v}_{opt}$ with Eq. (7)
  Compute deflection $\delta\mathbf{x}_b$ with Eq. (1)
  $\mathbf{S} = []$
  for $fe \in FE$ **do**
    Add $\delta\mathbf{x}_b$ to the FE limits on b parameter components:
      $\underline{\boldsymbol{u}}_{fe} = \underline{\boldsymbol{u}}_{fe} + [\delta x_b(1), \delta x_b(3), 0, 0, 0]$
      $\overline{\boldsymbol{u}}_{fe} = \overline{\boldsymbol{u}}_{fe} + [\delta x_b(1), \delta x_b(3), 0, 0, 0]$
    $\mathbf{u}_{fe} = \arg\max_{\mathbf{u}\in\Omega_{fe}}(P_C; \delta\mathbf{x}_b)$
    $\mathbf{S} = \mathbf{S} + \mathbf{\Sigma}_{fe}$
  end
  Compute P_C with Eq. (4)
  $\Delta P_C = abs(P_C - P_{C_1})$
  $P_{C_1} = P_C$
end

Min-max impulsive magnitude optimisation algorithm

Algorithm 2: Min-max impulsive CAM optimisation algorithm, accounting for magnitude optimisation.

Initialise $\epsilon_{Pc}, \Delta P_C, \delta v_{step}$
$\mathbf{S} = []$
for $fe \in FE$ **do**
  $\mathbf{u}_{fe} = \arg\max_{\mathbf{u}\in\Omega_{fe}}(P_C)$
  $\mathbf{S} = \mathbf{S} + \mathbf{\Sigma}_{fe}$
end
Compute P_{C_1} with Eq. (4)
while $\Delta P_C > \epsilon_{Pc}$ **do**
  $\mathcal{T} = \mathbf{QT}^T\mathbf{S}^{-1}\mathbf{TQ}$
  Compute $\mathbf{d}_{opt}$ with Eq. (7)
  $\delta v_{opt} = \delta v_{max}$
  Compute P_C with Eq. (4)
  while $P_C < P_{C0}$ **do**
    $\delta\mathbf{v}_{opt} = \delta v_{opt}\mathbf{d}_{opt}$
    Compute deflection $\delta\mathbf{x}_b$ with Eq. (1)
    $\mathbf{S} = []$
    for $fe \in FE$ **do**
      Add $\delta\mathbf{x}_b$ to the FE limits on b parameter components:
        $\underline{\boldsymbol{u}}_{fe} = \underline{\boldsymbol{u}}_{fe} + [\delta x_b(1), \delta x_b(3), 0, 0, 0]$
        $\overline{\boldsymbol{u}}_{fe} = \overline{\boldsymbol{u}}_{fe} + [\delta x_b(1), \delta x_b(3), 0, 0, 0]$
      $\mathbf{u}_{fe} = \arg\max_{\mathbf{u}\in\Omega_{fe}}(P_C; \delta\mathbf{x}_b)$
      $\mathbf{S} = \mathbf{S} + \mathbf{\Sigma}_{fe}$
    end
    Compute P_C with Eq. (4)
    $\delta v_{opt} = \delta v_{opt} - \delta v_{step}$
  end
  $\Delta P_C = abs(P_C - P_{C_1})$
  $P_{C_1} = P_C$
end

Low-thrust CAM optimisation

Algorithm 3: Low-thrust optimisation algorithm.

Initialise $\delta v_{max}, \varepsilon_{max}, \theta_m$
Stage 1: Optimal direction, acceleration magnitude and arc-length:
  $\delta v_{opt} = \delta v_{max}$
  $\boldsymbol{d}_{opt}|_{\theta_m}$, using Algorithm 1
  $\Delta\theta_m = 2\,(\theta_c - \theta_m)$
  $\theta_{mf} = \theta_c$
  $\theta_{m0} = \theta_{mf} - \Delta\theta_m$
  $\Delta t_b = f_1(\Delta\theta_m, \theta_m, \theta_c)$
  $\varepsilon_{opt} = \varepsilon_{max}$
Stage 2: Deflection at b-plane, $\delta\mathbf{x}_b$:
  Propagate modified orbit to TCA:
  if $\theta_{mf} = \theta_c$ **then**
    Use Fable with ε_{opt} and $\boldsymbol{d}_{opt}$ from θ_{m0} to θ_c
  else
    Use Fable with ε_{opt} and $\boldsymbol{d}_{opt}$ from θ_{m0} to θ_{mf}
    Propagate coast-arc ($\varepsilon = 0$) from θ_{mf} to θ_c
  end
  Compute deflection:
    Project state on b-plane
    Nominal miss distance after CAM: $\mathbf{r}_{e_{LT}}$
    $\delta\mathbf{x}_b = \mathbf{r}_{e_{LT}} - \mathbf{r}_{e_0}$
Stage 3: Worst-case scenario after CAM:
  $\boldsymbol{u}_{WC_{LT}} = \boldsymbol{u}_{WC} + [\delta x_b(1), \delta x_b(3), 0, 0, 0]$

Low-thrust CAM fuel saving optimisation: acceleration reduction

Algorithm 4: Low-thrust optimisation algorithm. Fuel saving via acceleration minimisation.

```
Initialise δv_max, ε_max, δε, θ_m, P_C0
Call Algorithm 3
if P_C < P_C0 then
    while P_C < P_C0 and ε_opt > 0 do
        ε_opt = ε_opt − δε
        Call Stage 2 and Stage 3 of Algorithm 3
        Compute P_C = f(ε_opt, u_WC_LT, d_opt, Δθ_m)
    end
end
```

Low-thrust CAM fuel saving optimisation: burning-time reduction

Algorithm 5: Low-thrust optimisation algorithm. Fuel saving via burning-time minimisation.

```
Initialise δv_max, ε_max, δθ, θ_m, P_C0
Call Algorithm 3
if P_C < P_C0 then
    while P_C < P_C0 and ε_opt > 0 do
        θ_m0 = θ_m0 + δθ
        θ_mf = θ_mf − δθ
        Δθ_m = θ_mf − θ_m0
        Call Stage 2 and Stage 3 of Algorithm 3
        Compute P_C = f(ε_opt, u_WC_LT, d_opt, Δθ_m)
    end
end
```

Acronym

ANN: Artificial Neural Networks
bpa: basic probability assignment
CAM: Collision Avoidance Manoeuvre
CDM: Conjunction Data Message
DSt: Dempster-Shafer theory of evidence
FE: Focal Element
HBR: Hard-Body Radius
ICS: Intelligent Classification System
LT: Low-Thrust
MAE: Maximum Absolute Error
ML: Machine Learning
MC: Monte Carlo
PoC: Probability of Collision
RF: Random Forests
RMSE: Root Mean Squared Error
STM: Space Traffic Management
TCA: Time of Closest Approach

References

Abay, R., 2017. Collision avoidance dynamics for optimal impulsive collision avoidance maneuvers. In: Proceedings of the 8th International Conference on Recent Advances in Space Technologies (RAST), pp. 263–271.

Abay, R., Brown, M., Boyce, R., Karacor, A., 2017. Open Source Collision Avoidance Maneuver Planning Tool. 68th International Astronautical Conference, Adelaide, Australia. 25–29 September. Paper number: IAC-17, A6,7,3, x38098.

Alfano, S., 2004. Relating position uncertainty to maximum conjunction probability. J. Astronaut. Sci. 53, 193–205.

Balch, M., Martin, R., Ferson, S., 2019. Satellite conjunction analysis and the false confidence theorem. Proc. Roy. Soc. A: Mathe., Phys. Eng. Sci. 475. Paper number: 20180565.

Bastida Virgili, B., Flohrer, T., Krag, H., Merz, K., Lemmens, S., 2019. CREAM — ESA's Proposal for Collision Risk Estimation and Automated Mitigation. 1st International Orbital Debris Conference, Sugar Land, Texas, United States. 9-12 December. Paper number: 6031.

Bombardelli, C., Hernando-Ayuso, J., 2015. Optimal Impulsive Collision Avoidance in Low Earth Orbit. J. Guidance Control Dyn. 38 (2), 217–225.

Breiman, L., 2001. Random forest. Machine Learn. 45, 5–32.

Di Carlo, M., Romero Martin, J., Vasile, M., 2018. Camelot - computational-analytical multi-fidelity low-thrust optimisation toolbox. CEAS Space J. 10, 25–36.

ESA, 2019. Kelvins collision avoidance challenge. https://kelvins.esa.int/collision-avoidance-challenge/home/.

Filippi, G., Vasile, M., 2019. A Memetic Approach to the Solution of Constrained Min-Max Problems. IEEE CEC 2019, Wellington, New Zealand. 10–13 June, 506–513.

Gonzalo, J., Colombo, C., Di Lizia, P., 2019. A semi-analytical approach to low-thrust collision avoidance manoeuvre design. In: 70th International Astronautical Congress, Washington D.C., United States. 21–25 October. Paper number: IAC-19-A6.2.3.

Gonzalo, J., Colombo, C., Di Lizia, P., 2020. Introducing MISS, a new tool for collision avoidance analysis and design. J. Space Saf. Eng. 7, 282–289.

Greco, G., Sanchez, L., Manzi, M., Vasile, M., 2021. A Robust Bayesian Agent for Optimal Collision Avoidance Manoeuvre Planning. 8th European Conference on Space Debris, ESA/ESOC, Darmstadt, Germany. 20-23 April.

Hernando-Ayuso, J., Bombardelli, C., 2020. Low-Thrust Collision Avoidance in Circular Orbits. J. Guidance Control Dyn. 44 (5), 983–995.

Kubat, M., 2017. An Introduction to Machine Learning, 2nd Edition. Springer Publishing Company, Incorporated, Cham, Switzerland.

Mashiku, A., Frueh, C., Memarsadeghi, N., 2018. Supervised-machine Learning for Intelligent Collision Avoidance Decision-making and Sensor Tasking. 2018 NASA Goddard Workshop on Artificial Intelligence.

Mashiku, A., Frueh, C., Memarsadeghi, N., Gizzi, E., Zielinki, M., Burton, A., 2019. Predicting Satellite Close Approaches in the Context of Artificial Intelligence. AAS/AIAA Astrodynamics Specialist Conference, Portland, Maine, United States. 11–15 August.

Muelhaupt, T., Sorge, M., Morin, J., Wilson, R., 2019. Space Traffic Management in the New Space Era. J. Space Saf. Eng. 6, 80–87.

Nag, S., Murakami, D., Lifson, M., Kopardekar, P., 2018. System Autonomy for Space Traffic Management. 2018 IEEE/AIAA 37th Digital Avionics Systems Conference (DASC), London, United Kingdom. 23-27 September.

Nag, S., Murakami, D., Marker, N., Lifson, M., Kopardekar, P., 2021. Prototyping Operational Autonomy for Space Traffic Management. Acta Astronaut. 180, 489–506.

Peng, H., Bai, X., 2017. Limits of Machine Learning Approach on Improving Orbit Prediction Accuracy using Support Vector Machine. Advanced Maui Optical and Space Surveillance (AMOS) Technologies Conference, Wailea, Maui, Hawaii, United States. 19–22 September. Paper number: 15.

Peng, H., Bai, X., 2018a. Artificial Neural Network-Based Machine Learning Approach to Improve Orbit Prediction Accuracy. J. Spacecraft Rock. 55, 1248–1260.

Peng, H., Bai, X., 2018b. Improving Orbit Prediction Accuracy through Supervised Machine Learning. Adv. Space Res. 61 (10), 2628–2646.

Peterson, G., Sorge, M., Ailor, W., 2018. Space Traffic Management in the Age of Space Era. Center for Space Policy and Strategy.

Serra, R., Arzelier, D., Joldes, M., Lasserre, J., Rondepierre, A., Salvy, B., 2016. Fast and Accurate Computation of Orbital Collision Probability for Short-Term Encounters. J. Guidance Control Dyn. 39, 1–13.

Shafer, G., 1976. A Mathematical Theory of Evidence, 1st Edition. Princeton University Press, 1976, Princeton, NJ.

Sánchez, L., Vasile, M., 2020. AI for Autonomous CAM Execution. 71st International Astronautical Congress. The CyberSpace Edition. 12–14 October. Paper number: IAC–20–A6,2,12, x58045.

Sánchez, L., Vasile, M., 2021. On the Use of Machine Learning and Evidence Theory to Improve Collision Risk Management. Acta Astronaut. 181, 694–706.

Sánchez, L., Vasile, M., Minisci, E., 2019. AI to Support Decision Making in Collision Risk Assessment. 70th International Astronautical Conference, Washington, D.C., United States. 21–25 October. Paper number: IAC–19–A6, IP,20, x53728.

Stevenson, E., Rodriguez-Fernandez, V., Urrutxua, H., Morand, V., Camacho, D., 2021. Artificial Intelligence for All vs. All Conjunction Screening. 8th European Conference on Space Debris, ESA/ESOC, Darmstadt, Germany. 20-23 April.

Tulczyjew, L., Myller, M., Kawulok, M., Kostrzewa, D., Nalepa, J., 2020. Toward automated collision avoidance: Predicting the risk of satellite collisions using machine learning-powered technique. 71st International Astronautical Congress. The CyberSpace Edition. 12–14 October. Paper number: IAC-20, A6, VP,13, x57288.

Uriot, T., Izzo, D., Simões, L., Abay, R., Einecke, N., Rebhan, S., Martinez-Heras, J., Letizia, F., Siminski, J., Merz, K., 2022. Spacecraft collision avoidance challenge: Design and results of a machine learning competition. Astrodynamics 6, 121–140.

Vasile, M., Colombo, C., 2008. Optimal Impact Strategies for Asteroid Deflection. J. Guidance Control Dyn. 31 (4), 858–872.

Vasile, M., Rodriguez-Fernandez, V., Serra, R., Camacho, D., Riccardi, A., 2017. Artificial Intelligence in Support to Space Traffic Management. 68th International Astronautical Conference, Adelaide, Australia. 25–29 September. Paper number: IAC–17–A6,7,1, x41479.

Zuiani, F., Vasile, M., 2014. Extended analytical formulas for the perturbed keplerian motion under a constant control acceleration. Celestial Mech. Dyn. Astron. 121, 275–300.